Seasonality in aerodynamic resistance across a range of North American ecosystems

Adam M. Young [a,b,*], Mark A. Friedl [c], Bijan Seyednasrollah [a,b], Eric Beamesderfer [a,b], Carlos M. Carrillo [d], Li Xiaolu [d], Minkyu Moon [c], M. Altaf Arain [e], Dennis D. Baldocchi [f], Peter D. Blanken [g], Gil Bohrer [h], Sean P. Burns [g,i], Housen Chu [j], Ankur R. Desai [k], Timothy J. Griffis [l], David Y. Hollinger [m], Marcy E. Litvak [n], Kim Novick [o], Russell L. Scott [p], Andrew E. Suyker [q], Joseph Verfaillie [f], Jeffrey D. Wood [r], Andrew D. Richardson [a,b]

[a] School of Informatics, Computing, and Cyber Systems, Northern Arizona University, Flagstaff, AZ 86011, United States
[b] Center for Ecosystem Science and Society, Northern Arizona University, Flagstaff, AZ 86011, United States
[c] Department of Earth and Environment, Boston University, Boston, MA 02215, United States
[d] Department of Earth and Atmospheric Sciences, Cornell University, Ithaca, NY 14853, United States
[e] School of Earth, Environment & Society and McMaster Centre for Climate Change, McMaster University, Hamilton, ON, Canada
[f] Department of Environmental Science, Policy and Management, University of California, Berkeley, CA 94720, United States
[g] Department of Geography, University of Colorado, Boulder, CO 80309, United States
[h] Department of Civil, Environmental and Geodetic Engineering, The Ohio State University, Columbus, OH 43210, United States
[i] National Center for Atmospheric Research, Boulder, CO, 80301, United States
[j] Lawrence Berkeley National Laboratory, Berkeley, CA 94702, United States
[k] Department of Atmospheric and Oceanic Sciences, University of Wisconsin-Madison, Madison, WI 53706, United States
[l] Department of Soil, Water, and Climate, University of Minnesota, Saint Paul, MN 55108, United States
[m] Northern Research Station, USDA Forest Service, Durham, NH 03824, United States
[n] Biology Department, University of New Mexico, Albuquerque, NM 87107, United States
[o] O'Neill School of Public and Environmental Affairs, Indiana University - Bloomington. Bloomington, IN, 47408, United States
[p] Southwest Watershed Research Center, USDA-Agricultural Research Service, Tucson, AZ, United States
[q] School of Natural Resources, University of Nebraska, Lincoln, NE 68583, United States
[r] School of Natural Resources, University of Missouri, Columbia, MO 65211, United States

ARTICLE INFO

ABSTRACT

Surface roughness – a key control on land-atmosphere exchanges of heat and momentum – differs between dormant and growing seasons. However, how surface roughness shifts seasonally at fine time scales (e.g., days) in response to changing canopy conditions is not well understood. This study: (1) explores how aerodynamic resistance changes seasonally; (2) investigates what drives these seasonal shifts, including the role of vegetation phenology; and (3) quantifies the importance of including seasonal changes of aerodynamic resistance in "big leaf" models of sensible heat flux (H). We evaluated aerodynamic resistance and surface roughness lengths for momentum (z_{0m}) and heat (z_{0h}) using the kB^{-1} parameter ($\ln(z_{0m}/z_{0h})$). We used AmeriFlux data to obtain surface-roughness estimates, and PhenoCam greenness data for phenology. This analysis included 23 sites and ~190 site years from deciduous broadleaf, evergreen needleleaf, woody savanna, cropland, grassland, and shrubland plant-functional types (PFTs). Results indicated clear seasonal patterns in aerodynamic resistance to sensible heat transfer (R_{ah}). This seasonality tracked PhenoCam-derived start-of-season green-up transitions in PFTs displaying the most significant seasonal changes in canopy structure, with R_{ah} decreasing near green-up transitions. Conversely, in woody savanna sites and evergreen needleleaf forests, patterns in R_{ah} were not linked to green-up. Our findings highlight that decreases in kB^{-1} are an important control over R_{ah}, explaining > 50% of seasonal variation in R_{ah} across most sites. Decreases in kB^{-1} during green-up are likely caused by increasing z_{0h} in response to higher leaf area index. Accounting for seasonal variation in kB^{-1} is key for predicting H as well; assuming kB^{-1} to be constant resulted in significant biases that also exhibited strong seasonal patterns. Overall, we found that aerodynamic resistance can be sensitive to phenology in ecosystems having

* Corresponding author at: School of Informatics, Computing, and Cyber Systems, Northern Arizona University, Flagstaff, AZ 86011, United States.
E-mail address: adam.young@nau.edu (A.M. Young).

strong seasonality in leaf area, and this linkage is critical for understanding land-atmosphere interactions at seasonal time scales.

1. Introduction

The horizontal and vertical structure of vegetation creates an aerodynamically rough surface, generating mechanical turbulence that exerts significant control over aerodynamic resistance to heat transfer from the surface to the atmosphere (Brutsaert, 1982; Garratt and Hicks, 1973; Pitman, 2003; Verma, 1989). Surface roughness varies with land cover type (Lee et al., 2011), leaf area (Dolman, 1986; Raupach, 1994; Shaw and Pereira, 1982), and canopy height (Chu et al., 2018; Sonnentag et al., 2011), such that changes in vegetation structure lead to significant changes in aerodynamic resistance. Vegetation phenology triggers significant and rapid changes in the structure of the canopy (Richardson et al., 2013), altering surface roughness during green-up and senescence. Such phenology-driven impacts can influence the land-surface energy balance by changing aerodynamic resistance and hence sensible heat flux (H), in addition to other key biophysical processes such as evapotranspiration (Fitzjarrald et al., 2001; Moon et al., 2020; Schwartz, 1992). Capturing dynamics between phenology and aerodynamic resistance is therefore critical for accurately parameterizing the role of phenology in land-surface models (e.g., Richardson et al., 2012). More broadly, phenology driven changes in aerodynamic resistance can affect the atmospheric boundary-layer, including temperature profile development, boundary-layer height and cloud formation, and near-surface micro-climate (Baldocchi and Ma, 2013; Betts, 2004; Novick and Katul, 2020).

The magnitude of H is controlled by the difference between surface and air temperatures and the aerodynamic resistance to sensible heat transfer. Modeling and predicting aerodynamic resistance requires information on two key surface-roughness parameters: roughness lengths for momentum and heat (Verhoef et al., 1997). The roughness length for momentum (z_{0m}) defines the height above the surface that wind speed extrapolates to zero, and the roughness length for heat (z_{0h}) is the effective source height in the vertical temperature profile for sensible heat. In ecosystems with taller roughness obstacles (e.g., forests), an additional parameter is commonly needed: the zero-plane displacement height (d). Under such conditions, wind speed extrapolates to zero at height $d + z_{0m}$. Differences between z_{0m} and z_{0h} result in an "excess resistance" to heat transfer relative to momentum transfer. Specifically, heat transfer from $z_{0h} \rightarrow z_{0m}$ is dominated by molecular diffusion, while heat transfer above z_{0m} is controlled by more efficient processes associated with eddy diffusion (Bonan, 2016; Thom, 1972). In land-surface modeling, the parameter kB^{-1} ($\ln(z_{0m}/z_{0h})$) is used to quantify this excess resistance between z_{0m} and z_{0h} (Brutsaert, 1982; Owen and Thomson, 1963; Thom, 1972). Further details on the derivation of excess resistance and kB^{-1} are found in Section 2.1.

The kB^{-1} parameter varies significantly with land-cover type, leaf area, and other environmental variables (Brutsaert, 1982; Rigden et al., 2018). For example, a deciduous broadleaf forest acts as a permeable-rough surface, defined as having densely packed, porous elements and exhibiting relatively low kB^{-1} values (kB^{-1} generally ranges from 0–4). Conversely, in arid ecosystems, the canopy is characterized by uneven and sparse roughness elements (i.e., a bluff-rough surface), and kB^{-1} generally exhibits higher values (kB^{-1} ranges from 2–10) (Rigden et al., 2018). For bare soil, kB^{-1} has low values (ranging from 0-1), and negative kB^{-1} values have also been estimated (Yang et al., 2008). This variability in kB^{-1} among differing land cover implies differences in the physical arrangement and structure of surface-roughness elements strongly governs behavior of kB^{-1}. While this variability is well documented among varying land-cover, little work exists exploring seasonal changes in kB^{-1}, which may in part be driven by changes in canopy structure, including the amount and distribution of leaf area.

kB^{-1} displays strong temporal variability in response to multiple different environmental factors. At a diurnal scale for sparse canopies, solar radiation penetrates below the canopy, warming the soil, and causing z_{0h} to be effectively the height of the soil surface, thereby increasing kB^{-1}. Meanwhile, z_{0m} is constant at daily time scales (Brutsaert and Sugita, 1996; Kustas et al., 1989; Verhoef et al., 1997). At a seasonal time scale, some evidence suggests that changing leaf area over time causes a distinct negative relationship between leaf area index and kB^{-1} (Qualls and Brutsaert, 1996). These patterns can also be generalized for different time scales. Conceptually (Fig. 1), daily kB^{-1} peaks at midday as the diurnal cycle in solar radiation causes the magnitude of the temperature gradient at the top of the canopy to increase, ultimately altering z_{0h}. Similarly, the impact of vegetation green-up can also cause kB^{-1} to vary at seasonal time scales. For example, changes in z_{0h} may effectively track changes in z_{0m}, leading to a constant kB^{-1} for the entire season. Conversely, z_{0h} may increase faster relative to z_{0m}, leading to decreases in kB^{-1} during green-up transitions (Fig. 1).

Determining whether changes in z_{0m} or z_{0h} are the primary driver of seasonal variation in kB^{-1} is critical for identifying the biophysical drivers of aerodynamic resistance. A simple – and common – approach is to estimate z_{0m} based on mean canopy height (h_c) (e.g., $z_{0m} = 0.1h$; Bonan, 2016). d is similarly estimated as $d = 0.7h_c$. However, while this is a common method for estimating these roughness parameters, this approach has several important limitations. First, this approach cannot produce time series of changes in z_{0m} unless continuous measurements of h_c are recorded. Second, seasonal signals of estimated z_{0m} are complex and may not effectively track canopy height. For example, as the canopy fills in after leaf emergence, z_{0m} may display non-monotonic variation with leaf area, increasing in length before decreasing (Shaw and Pereira, 1982). Additionally, as leaf area increases, the coefficients mapping h_c to z_{0m} and d (e.g., $z_{0m}/h_c = 0.1$ and $d/h_c = 0.7$) are not constant and can decrease and increase, respectively (Sakai, 2000). Measurements of wind speed and turbulence from flux towers offer an alternative method for estimating z_{0m}. For example, if wind speed is available at multiple heights above the canopy, a vertical wind-speed profile can be used to estimate both d and z_{0m} (Monteith and Unsworth, 2008), and a similar approach may be used for z_{0h} using air temperature profiles. At towers where measurements are available at only one height, an effective or "aerodynamic" canopy height can be estimated using Monin–Obukhov similarity theory, and thereby allow for inference into changes in of d and z_{0m} (Chu et al., 2018; Pennypacker and Baldocchi, 2016). However, this approach requires explicit assumptions regarding d/h_c and z_{0m}/h_c. More details regarding Monin–Obukhov similarity theory and estimating z_{0m} and d can be found in sections 2.1 and 2.6.

Common approaches to parameterizing kB^{-1} in predictions of H include simple assumptions. One such assumption is $z_{0m} = z_{0h}$ (i.e., $kB^{-1} = 0$) (Campbell and Norman, 1998). While assuming $kB^{-1} = 0$ simplifies calculations of H, it can cause significant bias (Yang et al., 2008), and is therefore not commonly used. Another approach is to assume kB^{-1} is a non-zero constant. For example, $kB^{-1} \approx 2$ is a common assumption, and shows good performance during the growing season for agricultural and forested land-cover types (Garratt and Francey, 1978; Zhao et al., 2016).

Despite extensive literature focused on kB^{-1}, few studies have explored how aerodynamic resistance changes seasonally, what drives these changes, and what the consequences are of such variation in aerodynamic resistance for predicting seasonal patterns in H (e.g., Moon et al., 2020; Sugita and Kubota, 1994). Furthermore, estimates of H from vegetated surfaces in land-surface models directly rely on model assumptions linking surface roughness to changes in leaf area and canopy height, further motivating the need for clearer understanding of how phenology may influence surface roughness (Lawrence et al., 2019;

Zeng and Wang, 2007). Here, we address the following questions: (1) how does aerodynamic resistance change at seasonal time scales across a range of plant functional types and climate regimes, (2) what are the mechanisms that lead to changes in aerodynamic resistance, including the role of plant phenology, and (3) how does assuming kB^{-1} to be constant influence estimates of H at seasonal time scales? To address these questions, we analyzed data from 23 sites that are part of both the AmeriFlux and PhenoCam networks, covering deciduous broadleaf, evergreen needleleaf, cropland, grassland, woody savanna, and shrubland land-cover types, and spanning a broad climatological gradient across North America.

2. Materials and methods

2.1. Basic theory

Whole ecosystem H is commonly modeled using a "big leaf" approach, which considers that ecosystems behave as a single layer, and therefore does not account for vertical differences from the soil through the canopy (Knauer et al., 2018; Raupach and Finnigan, 1988). Under this "big leaf" approach, H is a function of the difference between the aerodynamic surface temperature (T_{aero}) and air temperature at tower height (T_a), as well as aerodynamic resistance to heat transfer (R_{ah}):

$$H = \frac{\rho c_p (T_{aero} - T_a)}{R_{ah}} \qquad (1)$$

where ρ is air density (kg m^{-3}) and c_p is a constant for the specific heat of dry air (1004.834 J K^{-1} kg^{-1}). The total aerodynamic resistance to heat transfer (R_{ah}; s m^{-1}) is the sum of the resistance to momentum transfer (R_{am}) and an excess resistance term (R_{bh}) representing differences between roughness lengths for momentum (z_{0m}) and heat (z_{0h}),

$$R_{ah} = R_{am} + R_{bh} \qquad (2)$$

To calculate R_{ah}, R_{am}, and R_{bh}, we used the methods described by Verma (1989) and published in the 'bigleaf' R package (Knauer et al., 2018). Specifically, we estimated R_{am} using the definition:

$$R_{am} = u / u_*^2 \qquad (3)$$

where u and u_* are tower-measured horizontal wind speed (m s^{-1}) and friction velocity (m s^{-1}), respectively. The excess resistance, R_{bh}, is defined as:

$$R_{bh} = \frac{1}{ku_*} \left[\ln\left(\frac{z_{0m}}{z_{0h}}\right) - \psi_h + \psi_m \right] \qquad (4)$$

Here, k is the unitless von Kármán constant (0.41), and ψ_m and ψ_h are stability functions for momentum and heat exchange using formulations from Dyer (1970) and Businger et al. (1971). Following Rigden et al. (2018) and Verma (1989), we used the common, simplified definition of R_{bh} ignoring stability effects over the short distance $z_{0m} \rightarrow z_{0h}$:
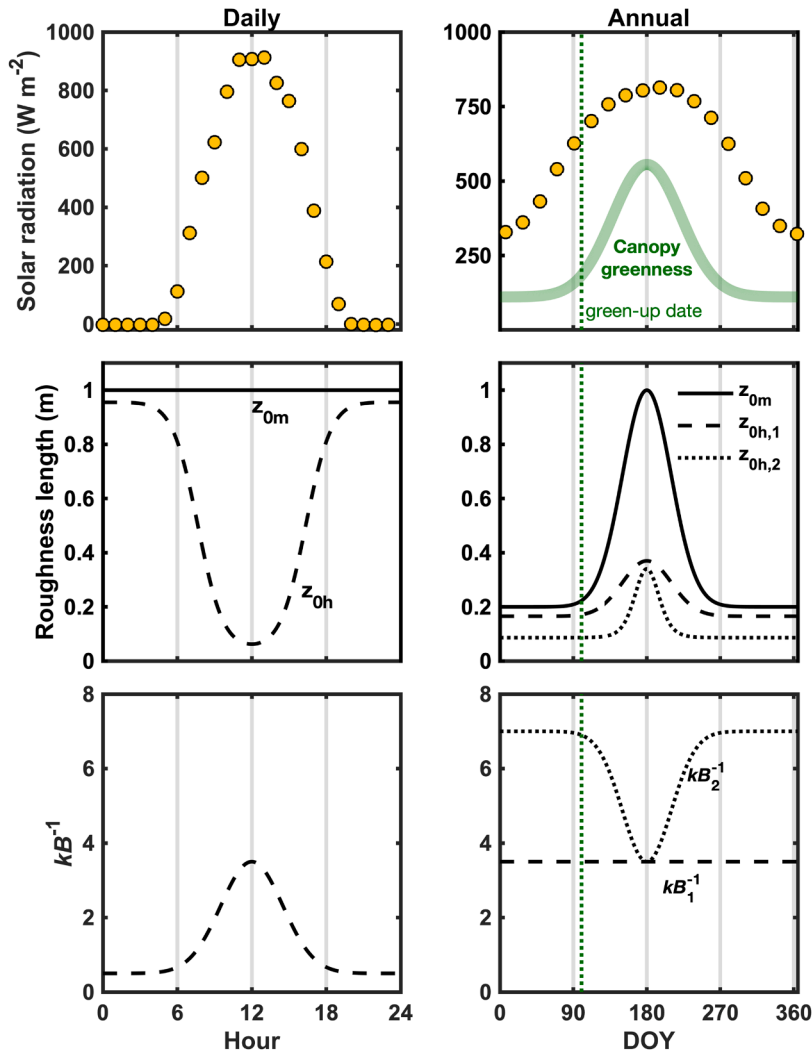

Fig. 1. Hypothesized behavior of kB^{-1} at multiple time scales. The left column of panels displays idealized diurnal behavior for short-statured vegetation at DOY 180 and how solar radiation may cause shifts in z_{0h} and kB^{-1}. Panels on the right-hand side depict behavior of kB^{-1} at a seasonal time scale. At seasonal time scales, the behavior of z_{0m} and z_{0h} relative to each other will determine kB^{-1}. Two different potential behaviors are depicted above. The dashed curve ($z_{0h,1}$) represents a potential scenario where z_{0h} proportionally tracks z_{0m} resulting in a constant kB^{-1} for the entire year. Alternatively, the dotted curve ($z_{0h,2}$) represents a scenario where z_{0h} increases faster relative to z_{0m} in response to green-up, resulting in a decrease in kB^{-1}. The faded green line represents canopy greenness while the vertical line indicates a theoretical green-up date. (For interpretation of the references to color in this figure legend, the reader is referred to the web version of this article.)

2.3. PhenoCam data

To capture vegetation phenology, we used the V2.0 PhenoCam public data release (Milliman et al., 2019; Seyednasrollah et al., 2019a; Seyednasrollah et al., 2019b). Here, we only provide a brief overview of PhenoCam data; a full description is presented in Richardson et al. (2018) and Seyednasrollah et al. (2019b). The PhenoCam network uses high-frequency imagery from digital cameras to track vegetation phenology. Following a standard protocol, cameras are mounted over-looking the vegetation of interest, and three-channel RGB images were recorded multiple times per day (typically every 30 min). For each site, a region-of-interest (ROI) in the image field-of-view is delineated to focus on the canopy. Using all pixels in this ROI, statistics summarizing RGB digital numbers (DN) are generated to quantify relative changes in canopy color over time. This canopy color information can be used to accurately identify phenological time series and transition dates (e.g., spring leaf emergence and fall senescence; Keenan et al., 2014). How-ever, canopy color from PhenoCam does not explicitly measure the physical structure of the canopy (e.g., LAI or roughness). In our analysis, we used time series of the green-chromatic coordinate (G_{CC}) to measure canopy greenness and extract transition dates,

$$G_{CC} = \frac{G_{DN}}{G_{DN} + R_{DN} + B_{DN}} \tag{9}$$

Daily values of G_{CC} were calculated from all daytime images under a 1- or 3-day moving-window (Sonnentag et al., 2012). The V2.0 data release provides four G_{CC} statistics for each moving window: mean, median, 75th percentile, and 90th percentile. In this analysis, we used the statistic that minimizes the root mean squared error (RMSE) between daily G_{CC} values and a locally weighted regression smoother (loess) at each site. The smoothing span for the loess curve was determined by minimizing a Bayesian Information Criterion (BIC) (Richardson et al., 2018), and the smoothed loess-derived values were further used to identify phenological transition dates. In our analysis, we used the 3-day moving window to visualize seasonal patterns in greenness and the 1-day product to estimate transition dates. This was necessary as tran-sition dates could not be identified in some of the dryland sites using the 3-day product. For this study, we used the start-of-season green-up date (i.e., "green-up") as our primary measure of spring phenology, as it characterizes the date of leaf emergence and acts as a clear separator between dormant and growing seasons. Specifically, this green-up date was equated to the day when 10% of the total seasonal amplitude in G_{CC} was reached. For evergreen needleleaf sites, changes in G_{CC} are caused by changes in foliage pigments on seasonal time scales, and are not related to changes in leaf area (Bowling et al., 2018; Seyednasrollah et al., 2021). The V2.0 release has been screened to remove low-quality imagery and image masks have been adjusted to account for camera field-of-view shifts. Only cameras set to fixed white balance were included, to remove negative impacts from auto-white balancing under default camera settings (Seyednasrollah et al., 2019b). Finally, we also conducted a brief supplementary comparison between G_{CC} time series and flux-tower derived estimates of broadband NDVI (e.g., Jenkins et al., 2007). We found strong similarities between these time series, indi-cating that PhenoCam G_{CC} can capture seasonal changes in vegetation that are also captured by radiometric measurements. Details on these comparisons are provided in Appendix S1 and Fig. S2. Additional met-adata information for each PhenoCam site, as well as example imagery and maps of vegetation cover, can be found in Table S1 and Fig. S3.

2.4. Estimating seasonal variation in aerodynamic resistance

We quantified R_{ah}, as well as the underlying components R_{am}, R_{bh}, and kB^{-1}, at a 3-day timestep to effectively visualize and identify po-tential seasonal patterns in these aerodynamic resistance terms among different ecosystems. First, we calculated R_{am} at a half-hour timescale using Eq. (3). Second, we used Eqs. (1) and (2) and our predictions of

R_{am} to estimate a single value of kB^{-1} that minimized prediction error of H across all half-hour values every three days. This value of kB^{-1} at a 3-day timestep allowed R_{bh} to be calculated using Eq. (7). Finally, we smoothed the time series for each variable using a loess curve. The span for the loess curve for each variable and site was optimized by mini-mizing the BIC, and this was the same method used for smoothing PhenoCam greenness data (see Section 2.3). By smoothing over a time series of non-overlapping 3-day estimates, our approach captures shifts occurring during phenological transitions, even under a short time duration. We chose a 3-day time scale for this averaging and subsequent smoothing because it was consistent with the time scale used with PhenoCam. We note that our method of estimating R_{bh} as a residual of R_{ah} and R_{am} will result in any errors in H being propagated into our estimates of R_{bh} and kB^{-1}. Errors in H could be derived from multiple sources, but are not likely a major concern. For example, it is possible that lack of energy balance closure could influence our results, especially if there is strong seasonality in the amount of closure occurring in concert with seasonal changes in the Bowen ratio. However, at the handful of sites where we examined this in detail, we found no evidence of strong seasonality in mid-day energy balance closure, and no emerging patterns that would allow us to link poor energy balance closure to strong seasonal variation in R_{bh}. Furthermore, while random or systematic measurement errors in H data could influence estimates of R_{bh}, our filtering approach was designed to minimize the impact of systematic errors (see Section 2.2) and by averaging mid-day fluxes over three days, the magnitude of random errors is also greatly reduced (e.g., Hagen et al., 2006; Hollinger and Richardson, 2005).

Any variable exhibiting strong seasonal variability will inherently have cyclical peaks and valleys. Here, we identified the timing of peaks and valleys for both R_{ah} and kB^{-1} (hereafter referred to as periods characterized by either "maximum" or "minimum" values, respectively). These maximum and minimum periods were then related to green-up. To do this, we first computed the 25th or 75th percentiles of the whole time series for each variable at each site. We then identified the days-of-year where each variable occurred above or below these 75th and 25th percentiles, equating these days to the timing of seasonal maximum and minimum values, respectively. The start-, middle-, and end-point for each maximum and minimum time period was identified by the 10th, 50th, and 90th percentiles across these day-of-year values. To calculate these relative day-of-year statistics, we used directional statistics using the *'circular'* package in R (Agostinelli and Lund, 2017). To visualize and compare the timing of seasonal transitions in R_{ah} and kB^{-1}, we plotted the transition dates for each of these variables against each other, as well as green-up date. The transition dates for R_{ah} and kB^{-1} used for this visualization were the "end" points (i.e., 90th percentile) of the distri-bution for timing maximum R_{ah} and kB^{-1} values, indicative of when kB^{-1} begins to decrease (e.g., see Figs. 3 and 5). Seasonal signals in kB^{-1} were much noisier compared to canopy greenness from PhenoCam, making it harder to precisely identify transition dates. Thus, our method here is undoubtedly accompanied by comparably higher uncertainty, and therefore transition dates for R_{ah} and kB^{-1} may not align with PhenoCam dates. Nevertheless, these values as transition dates are currently our best estimate of the timing of when R_{ah} or kB^{-1} begins to decrease, and are still valuable for exploring linkages between phenology and changes in aerodynamic resistance.

kB^{-1} is also frequently modeled as a response to the Reynolds roughness number (Re_*) (Rigden et al., 2018), where Re_* is defined as:

$$Re_* = \frac{z_{0m} u_*}{\nu} \tag{10}$$

Here, ν is the kinematic viscosity (Massman, 1999). Thus, we plotted kB^{-1} against Re_* for each season (dormant and growing) to visualize and compare our results more easily to past studies. For this simple visual-ization, we identified the growing season as those dates between the 50% green-up threshold and 50% green-down threshold (Richardson et al., 2018). The dormant season was identified as the period prior to

green-up.

2.5. Attribution analysis

We can attribute variability in R_{ah} to either R_{am} or R_{bh} (i.e., $R_{ah} = R_{am} + R_{bh}$; Eq. (2)), and understanding which of these factors has a stronger correspondence would provide key information to infer the primary drivers of R_{ah}. To conduct an attribution analysis, we used statistical properties defining the variance of the sum of two random variables (Rice, 2007),

$$Var(X + Y) = Var(X) + Var(Y) + 2Cov(X, Y) \tag{11}$$

Here, Var and Cov are the variance and covariance functions, respectively. We used Eq. (11) in combination with the relationship in Eq. (2) to attribute the relative contribution of total variance of R_{ah} or the covarying relationship between R_{am} and R_{bh},

$$Var(R_{ah}) = Var(R_{am} + R_{bh})$$

$$Var(R_{ah}) = Var(R_{am}) + Var(R_{bh}) + 2Cov(R_{am}, R_{bh}) \tag{12}$$

Calculations assumed N-1 degrees of freedom, with N being the number of independent 3-day periods. This analysis was done separately for each site using the unsmoothed time series.

2.6. Quantifying seasonal changes in surface roughness parameters

Seasonal shifts in kB^{-1} must be in response to either z_{0m} or z_{0h}. To help diagnose whether changes in kB^{-1} are associated with changes in z_{0m} or z_{0h}, we first quantified z_{0m} by estimating aerodynamic canopy height (h_a) at a 3-day timestep. We then use these patterns of z_{0m} in conjunction with kB^{-1} to infer how z_{0h} changes, ultimately allowing for inference into the drivers of kB^{-1}. For example, if kB^{-1} decreases while z_{0m} increases, we may infer those changes in z_{0h} are likely having a stronger influence on kB^{-1}, as increases in z_{0m} by itself should lead to increases in kB^{-1} (e.g., Fig. 1). z_{0m} is most commonly prescribed as simple functions of mean canopy height (h_c) (e.g., $z_{0m} = 0.1h_c$), with measured canopy heights reported by site PIs. However, z_{0m} has been shown to vary significantly with leaf area (Yang and Friedl, 2003), indicating physical h_c measurements may be limited at capturing seasonal changes in z_{0m}. Aerodynamic canopy height (h_a) offers an alternative to using observed h_c. Specifically, aerodynamic canopy height can be estimated using the Monin–Obukhov similarity theory definition of the log-wind profile,

$$u(z) = \frac{u_*}{k}\left[\ln\left(\frac{z - d}{z_{0m}}\right) - \psi_m\right] \tag{13}$$

Here, $u(z)$ is wind speed at height z, d is the zero-plane displacement height, and ψ_m is a stability function for momentum (Dyer and Hicks, 1970). Under near-neutral atmospheric stability (i.e., $\psi_m \approx 0$), Eq. (13) can be re-arranged to determine a single value of h_a that best predicts flux-tower measurements of $\frac{ku(z)}{u_*}$ using the assumptions that $d = 0.7h_a$ and $z_{0m} = 0.1h_a$,

$$\frac{ku(z)}{u_*} = \ln\left(\frac{z - 0.7h_a}{0.1h_a}\right) \tag{14}$$

While $d/z_{0m} = 7$ is a common assumption (Bonan, 2016), this ratio has been demonstrated to change with land-cover type, LAI, and stand density (Nakai et al., 2008). However, we maintained this assumption for our analysis, as we were primarily interested in simply understanding how h_a (and hence z_{0m}) changes seasonally; thus, the absolute accuracy of our h_a estimates was not critical.

To quantify seasonal variability in h_a, we first split up the time series at each site into non-overlapping 3-day windows. Within each window, a single value of h_a was optimized to minimize the mean absolute error between all observed and predicted half-hour values of $\frac{ku(z_r)}{u_*}$. This gave

us one estimate of h_a every three days. For this optimization, we used a different data filtering approach than in Section 2.2. Here, we closely followed Pennypacker and Baldocchi (2016) and Chu et al. (2018). Additionally, we filtered for atmospheric neutrality, and this was the only part of our analysis to include this filter. In estimating h_a, we applied a roughness sublayer correction at forest sites (Chu et al., 2018). If the reference height (z_r) was less than $1.5h_c$ (h_c equal to PI reported canopy height), we included a roughness-sublayer correction factor (λ_{rs}), optimizing using the following instead of Eq. (14):

$$\frac{ku(z)}{u_*} = \ln\left(\frac{z - 0.7h_a}{0.1h_a}\right) + \ln(\lambda_{rs}) \tag{15}$$

From Chu et al. (2018), $\lambda_{rs} = 1.25$. We did not include a roughness sublayer correction in any other part of our analysis, and we believe this would not meaningfully impact our results as Hu et al. (2020) found that including a roughness-sublayer correction did not improve predictions of turbulent fluxes. Seasonal summaries for h_a for each site are provided in Fig. S4.

In addition to calculating h_a, we also used wind-profile data from sites recording wind speed at multiple heights to individually estimate d and z_{0m}, independent of assumptions related to canopy height, such as $z_{0m} = 0.1h_c$ (sites with profile data availability are listed in Table 1). Specifically, we chose three sites for this analysis: US-MMS, US-Syv, and US-Ne1. We chose sites for this analysis based on whether d was likely to have significant influence in the wind profile, and on the availability of relatively complete and suitable time series of wind speed at two heights. To conduct this analysis, we used the difference between wind speeds at two different heights under near-neutral stability to find a single value of d that best predicts the left-hand side of Eqn (16) (Monteith and Unsworth, 2008):

$$\frac{k(u_1 - u_2)}{u_*} = \log\left(\frac{z_1 - d}{z_2 - d}\right) \tag{16}$$

Here, subscripts refer to two different measurement heights, with $z_1 > z_2$. Using this estimate of d, we were able to invert Eq. (13) to obtain an estimate of z_{0m}:

$$z_{0m} = \frac{z - d}{\exp\left\{\frac{ku(z)}{u_*}\right\}} \tag{17}$$

2.7. Seasonal sensitivity to estimating H

While initial results indicated there was significant seasonality in both R_{ah} and kB^{-1} (Figs. 2, 3, 6), it is also common to assume $kB^{-1} = 0$ or kB^{-1} is equal to a constant value (i.e., $kB^{-1} = c$) when predicting H. To understand the implications of using either of these assumption for predicting seasonal patterns in H, we calculated the relative difference between estimated ($\hat{H}$) and measured values of H (i.e., $\hat{H}/H$). The constant value c for each PFT was obtained from Rigden et al. (2018), and is representative of mean growing season kB^{-1}. The impacts of each assumption were evaluated by visualizing time series of the relative difference between measured and estimated H at a 3-day timestep.

3. Results

3.1. Seasonal variability in aerodynamic resistance

There were significant seasonal patterns in R_{ah} at most of our study sites, which spanned a continental-scale precipitation gradient (Fig. 2). In general, PFTs that exhibited the largest seasonal changes in leaf area (i.e., deciduous broadleaf, grassland, croplands) consistently produced strong seasonal signals in R_{ah} (Fig. 2). For example, at the wettest grassland site, a restored prairie landscape in the upper Midwest (US-Ro4, MAP = 879 mm; Markland, 2019), R_{ah} ranged from 44 s m^{-1} in the dormant season to 21 s m^{-1} in the growing season (Fig. 2). Likewise, at
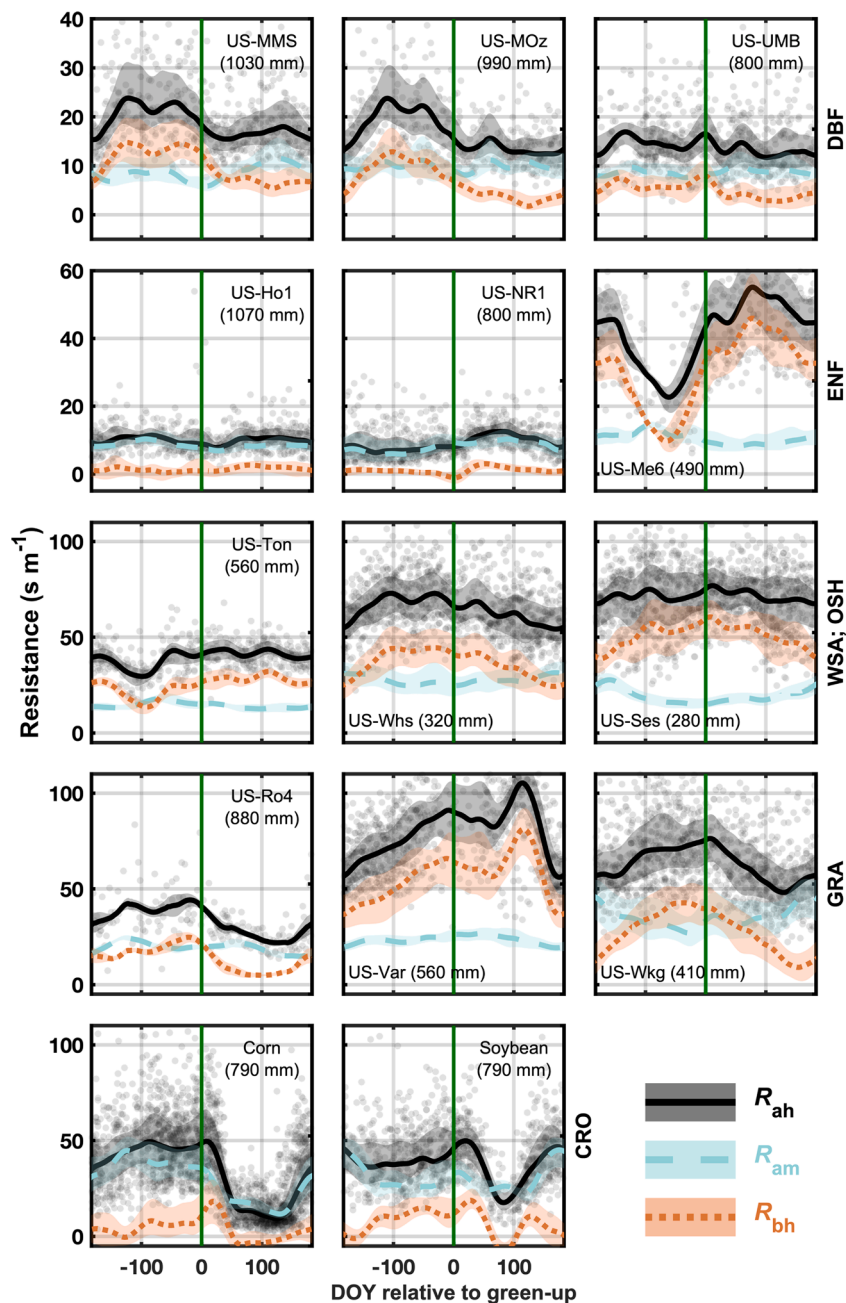
Fig. 2. Seasonal changes in R_{ah}, R_{am}, and R_{bh} from example sites for each PFT. For each site, the median is calculated for each DOY across all years, and these statistics are then smoothed using a loess smoother. Confidence bounds represent the interquartile range across all years as well (25th–75th percentiles). Mean annual precipitation is in parentheses. The plotted points are the unsmoothed data for R_{ah}. Plots for additional sites can be found in Fig. S5.

our driest grassland site, Kendall grassland in the Walnut Gulch Experimental Watershed of southern Arizona (US-Wkg, MAP = 340 mm; Scott et al., 2010), R_{ah} ranged from 75 s m^{-1} to 48 s m^{-1} (Fig. 2).

We further evaluated seasonal patterns by identifying the periods of the year when R_{ah} values were characteristically lower (i.e., at a "minimum") or higher (i.e., at a "maximum"). We found that in many cases maximum and minimum R_{ah} values occurred in distinct and non-overlapping periods, indicating strong seasonality (Fig. 3). Specifically, we found that maximum R_{ah} occurred prior to or during green-up, while minimum R_{ah} occurred after green-up at most deciduous broadleaf forests, grasslands, shrublands, and agricultural sites (Figs. 2, 3, and S6). For example, at a set of three agricultural sites at the University of Nebraska Agricultural Research and Development Center (US-Ne1, US-Ne2, and US-Ne3; Suyker and Verma, 2010; Suyker and Verma, 2012),

we found that maximum R_{ah} occurred from 120 days prior to green-up through 20 days after green-up for corn (*Zea mays* L.), while minimum R_{ah} ranged from 66 to 143 days after green-up. Similarly, for soybean (*Glycine max* [L.] Merr.), maximum R_{ah} ranged from 197 days prior to green-up through 8 days after green-up (Fig. S6).

We also observed seasonality in R_{ah} among some, but not all, evergreen-needleleaf and woody savanna sites. Wetter evergreen and savanna sites, as measured by mean annual precipitation (Table 1), displayed little seasonal variability in R_{ah}, while drier evergreen and savanna sites with lower stand density had some of the strongest seasonal patterns in R_{ah}. For example, US-Ho1 (MAP = 1070 mm), a sub-boreal, closed canopy site in Maine with ≈15–20% annual needle turnover (Hollinger et al., 1999), exhibited little seasonal variation in R_{ah}, R_{am}, or R_{bh} (Fig. 2), and R_{ah} had a seasonal amplitude of only 4 s

Fig. 3. Timing of seasonal maximum and minimum values for aerodynamic resistance to heat transfer (R_{ah}). Red and blue histograms display the empirical distribution of the seasonal maximum or minimum timing, respectively. Specifically, the histograms are for day of year values (relative to 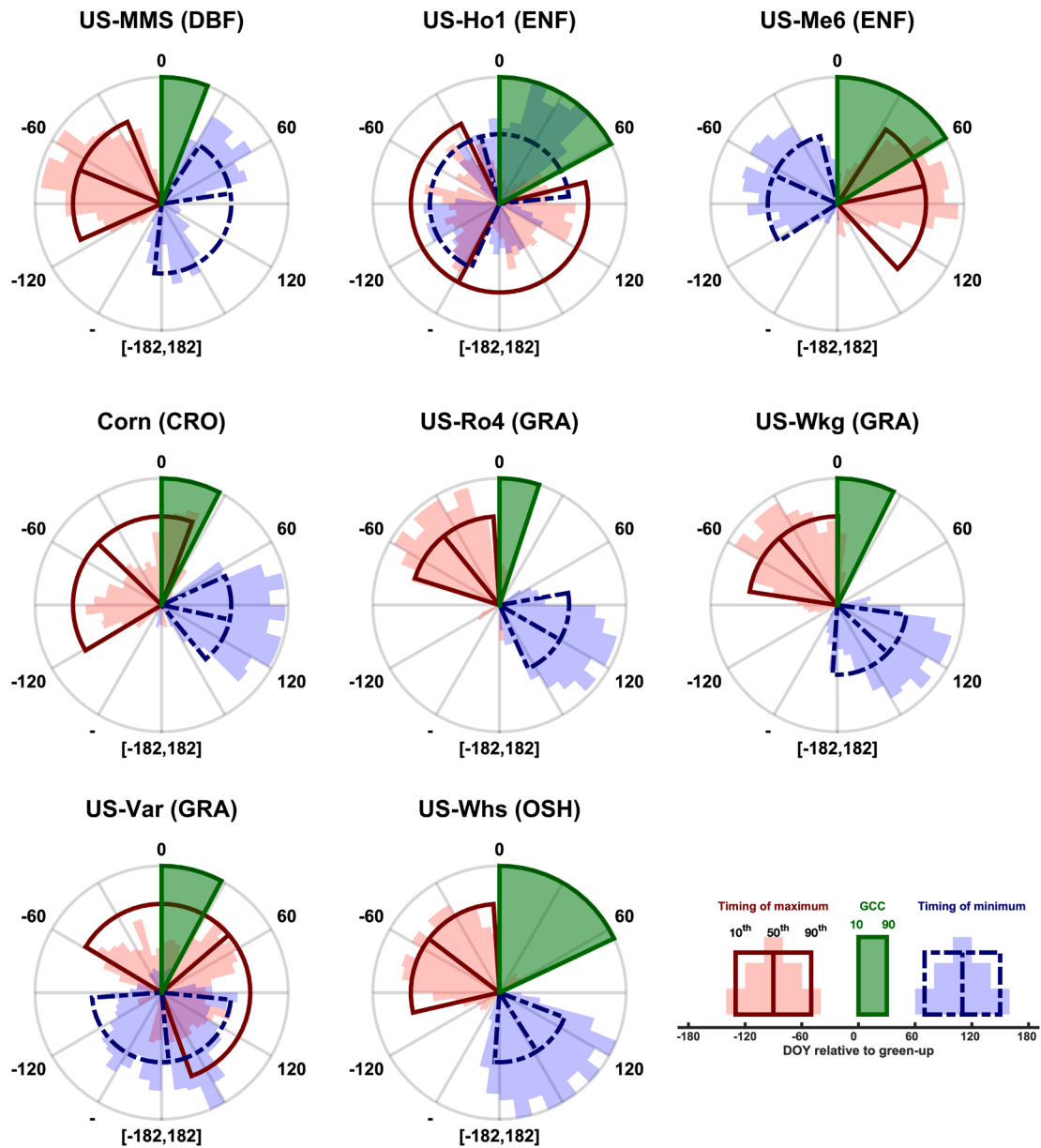green-up) for all days that were either above the 75th percentile (i.e., maximum) or below the 25th percentile (minimum). Day 0 (at the top of each plot) represents green-up. These empirical distributions of maximum or minimum timings are summarized by the 10th, 50th, and 90th percentiles of these relative day-of-year values as the beginning, middle, and end points, respectively (i.e., the red and blue "slices"). The green "slices" represent the green-up phenological transition period, bounded by dates when the G_{CC} curve reaches 10% and 90% of the total seasonal amplitude of G_{CC}. Plots for additional sites can be found in Fig. S6. (For interpretation of the references to color in this figure legend, the reader is referred to the web version of this article.)

m^{-1}. In comparison, at the lower stand density Metolius young burn site in central Oregon (US-Me6, MAP = 494 mm; Ruehr et al., 2014) or the Pinyon-Juniper woody savanna site in central New Mexico (US-Mpj, MAP = 385 mm; Anderson-Teixeira et al., 2011), we observed some of the largest seasonal changes in R_{ah} among all study sites, with seasonal amplitudes of 33 and 16 s m^{-1}, respectively (Fig. 2). Furthermore, the timing of minimum and maximum R_{ah} values at these drier evergreen needleleaf and savanna sites was opposite to the patterns found at deciduous broadleaf forests, with maximum R_{ah} occurring during the growing season and minimum values more prevalent during the dormant season prior to green-up (Figs. 2, 3, and S6).

3.2. Inferred drivers of R_{ah} seasonality and linkages to spring phenology

Our findings suggested that seasonal variability in R_{ah} was primarily attributable to changes in R_{bh}, not R_{am}, at most of our study sites. In general, there was strong correlation in the seasonal patterns of R_{ah} and R_{bh}, but much lower correspondence between R_{ah} and R_{am} (Fig. 2). For example, at US-MMS, a 90-100 year old deciduous broadleaf forest in southern Indiana (Dragoni et al., 2011), there was a well-defined decrease in R_{ah} near green-up, shifting from 23 s m^{-1} to 15 s m^{-1} (Fig. 2). This shift in R_{ah} directly tracked R_{bh}, which shifted from 15 s m^{-1} to 7 s m^{-1}. Conversely, R_{ah} was anti-correlated with R_{am} (Fig. 2). These patterns and linkages between R_{ah} and R_{bh} were reinforced by results from our attribution analysis where the total variance in R_{ah} was partitioned between R_{am}, R_{bh}, and the covariance between R_{am} and R_{bh}
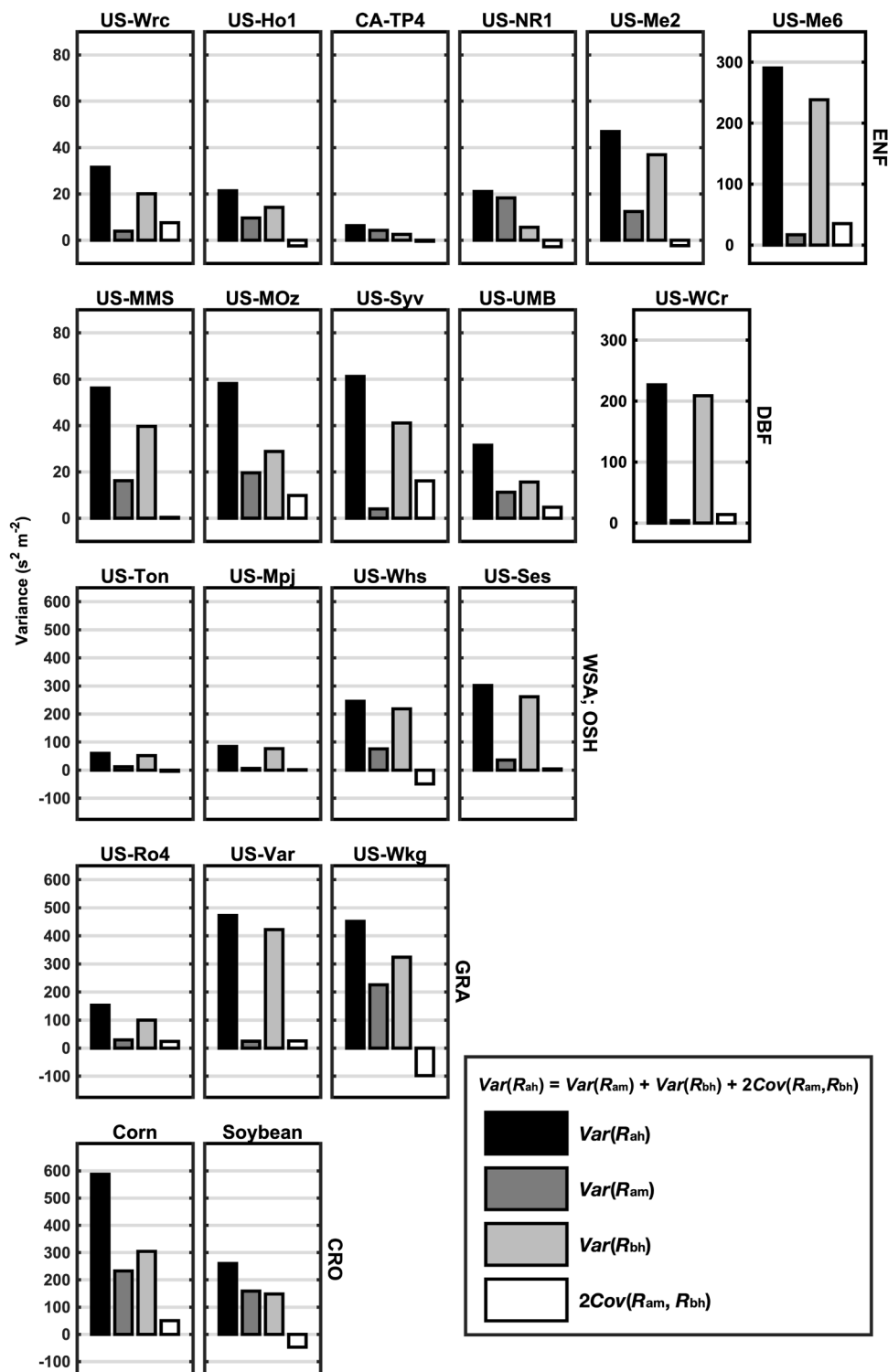
Fig. 4. Attribution of the total seasonal variance in R_{ah} to either R_{am}, R_{bh}, or $2Cov$ (R_{am}, R_{bh}). Corn and soybean data are obtained from US-Ne1, US-Ne2, and US-Ne3.

(Fig. 4). We found clear evidence among non-agricultural PFTs that the total variance in R_{ah} was primarily explained by R_{bh}, not R_{am} (Fig. 4). For example, across all deciduous broadleaf sites, variance in R_{bh} explained 42-87% of the total variance in R_{ah} compared to R_{am} (2–36%) (Fig. 3). There were only two non-agricultural sites where we found evidence for R_{am} having higher explanatory power than R_{bh}: CA-TP4 and US-NR1 (e.g., 63% vs 37% for CA-TP4) (Fig. 4).

Seasonal variation in R_{bh} is attributable to seasonal shifts in kB^{-1} rather than u_* (Eq. (7)), as u_* exhibits considerably less seasonal

variability. We found distinct and corresponding seasonal cycles between R_{bh} and kB^{-1} occurring at many sites (Figs. 2, 5, and 6); kB^{-1} generally reached its highest values immediately prior to or during green-up, followed by decreases during the transition to the growing season at deciduous broadleaf, grassland, shrubland, and agricultural sites (Figs. 5 and 6). At drier evergreen needleleaf sites, such as US-Me6, we found the opposite pattern, with kB^{-1} lower during the dormant season and increasing during the growing season (Figs. 5 and 6), with strong similarity to the signal in R_{ah} found at these same sites (Figs. 2
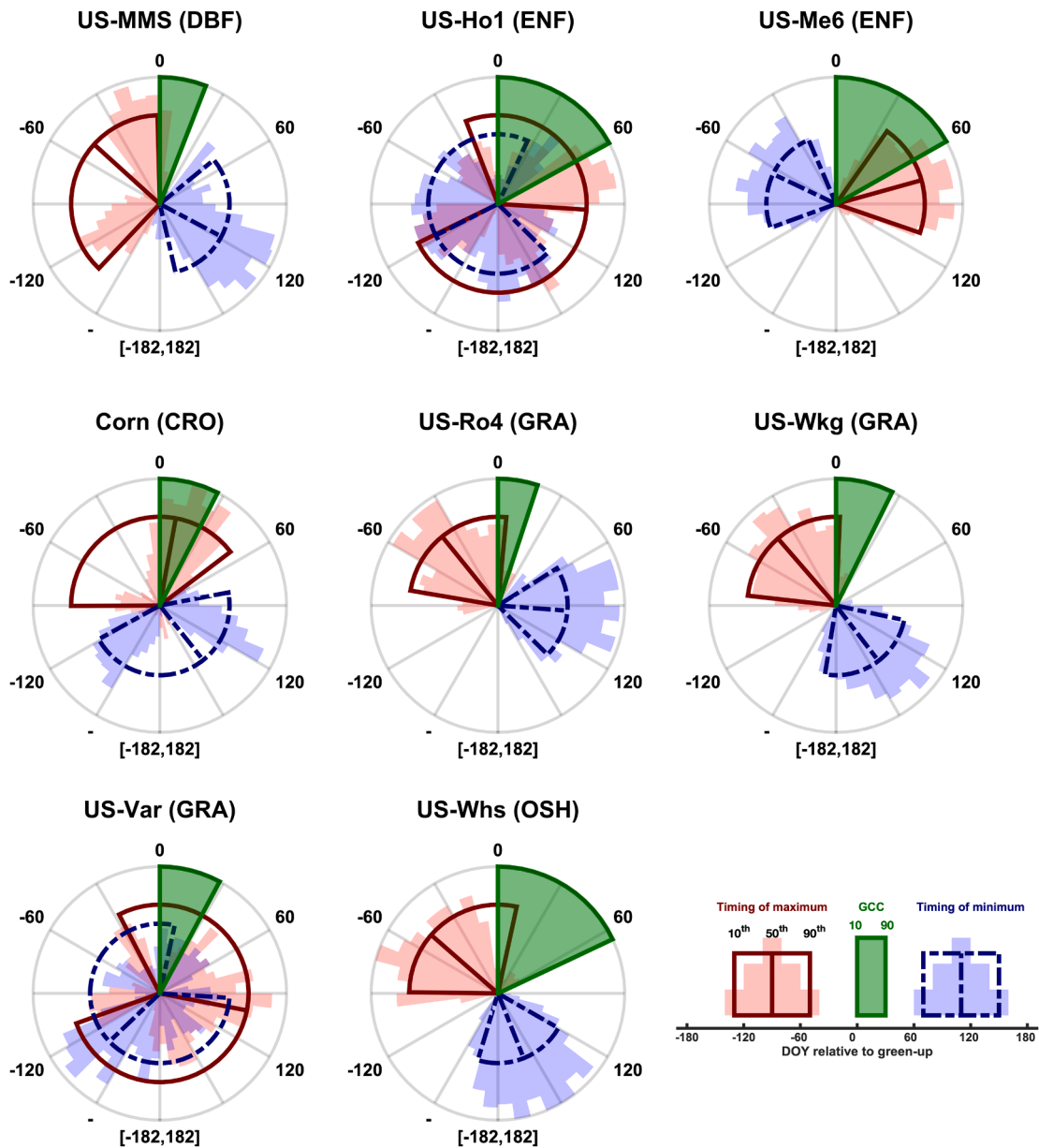
Fig. 5. Same as Fig. 3 but for kB^{-1}.

and 3). When comparing Figs. 3 and 5, we observe that a deciduous broadleaf site (US-MMS) the timing of maximum R_{ah} and kB^{-1} overlapped considerably. Similar patterns can be found at the other end of the precipitation gradient; at a shrubland site in southern Arizona (US-Whs), the median day-of-year of peak R_{ah} and kB^{-1} were almost identical: 43 and 45 days prior to start-of-season green-up (Figs. 3 and 5). When comparing all sites, we found a strong positive linear relationship between the transition dates for R_{ah} and kB^{-1}, with the transition dates for R_{ah} and kB^{-1} occurring within 30 days of each at 60% of all sites (Fig. 7a).

The timing of seasonal shifts in R_{ah} and kB^{-1} appeared to track green-up transition dates for some, but not all, sites (Fig. 7b,c). Linkages between green-up dates and shifts from higher to lower R_{ah} and kB^{-1} were notable at most deciduous broadleaf, grassland, and at least one shrubland site. For example, there were distinct decreases in kB^{-1} at two deciduous forest sites (US-MMS and US-MOz) immediately after spring green-up occurred, and this response was consistent even when green-up occurred approximately 30-days earlier than normal in 2012 (Fig. 6). This strong association between transition dates is visualized in Fig. 7b,

c; transition dates between kB^{-1} and G_{cc} occurred within 30 days of each other for 80% of deciduous broadleaf, two out of three of grassland, and one of two of shrubland sites. By comparison, for many evergreen needleleaf forests and woody savanna ecosystems, kB^{-1} transition dates generally occurred more than 120 days from green-up, if at all. In general, these patterns between kB^{-1} and greenness were comparable to the patterns we found for R_{ah}.

Finally, to help understand which surface roughness parameter (z_{0m} or z_{0h}) is driving kB^{-1} changes, we estimated d and z_{0m} through aerodynamic canopy height (h_a) and wind-profile data. In general, we found that h_a increases during the growing season, implying z_{0m} is also increasing (Fig. S4). We found a similar pattern for a cropland site with corn (US-Ne1), where there was a distinct increase in both d and z_{0m} during the growing season (Fig. 8). While this pattern occurred at most sites, we also found examples where z_{0m} decreased during the growing season, indicating that the canopy became smoother. Specifically, at US-MMS and US-Syv, z_{0m} decreased by approximately 1.5 m during the transition from spring to summer (Figs. 8 and S4).
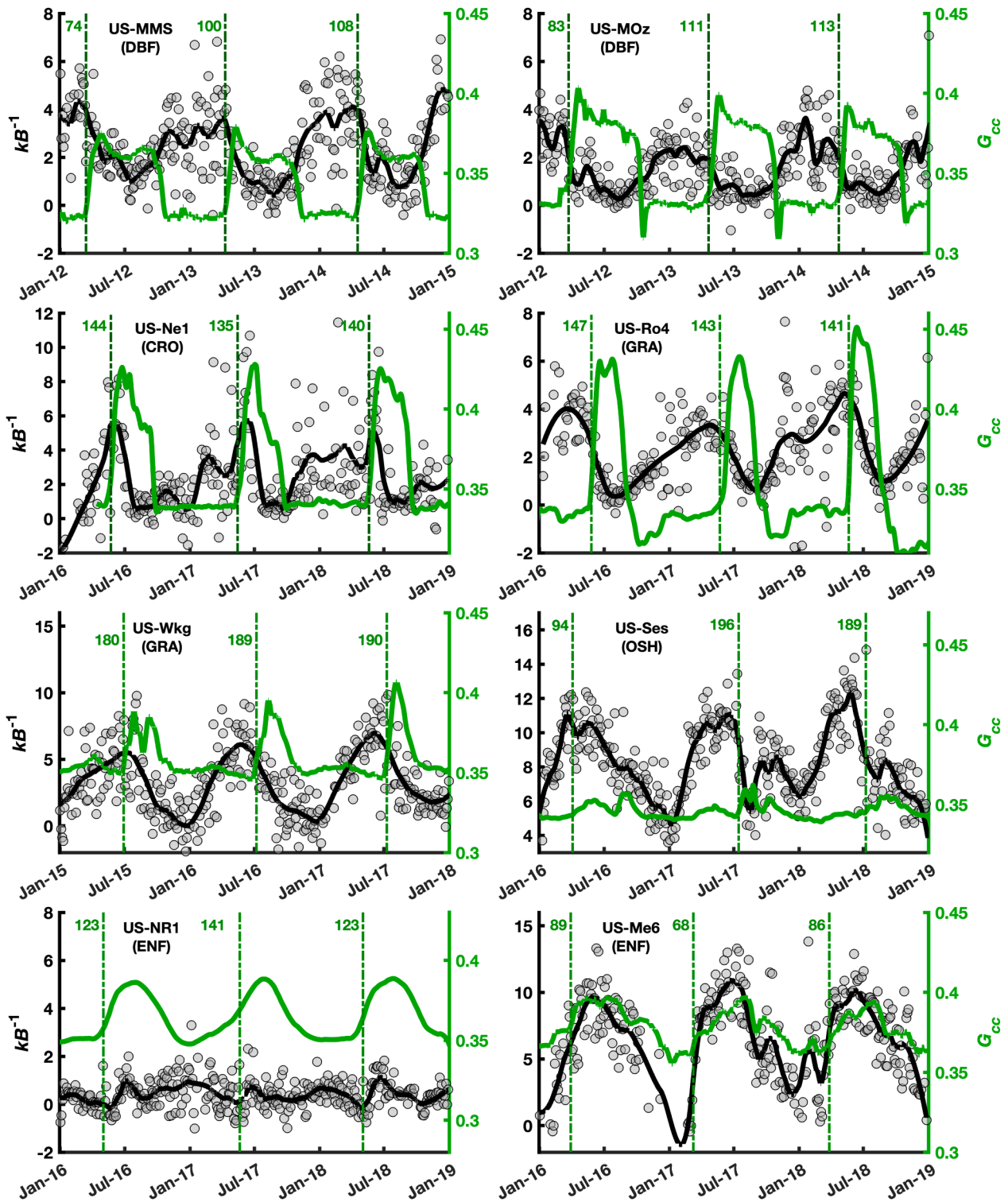
Fig. 6. Time series for kB^{-1} and G_{cc} for a range of different PFTs. Each panel covers a time period of three years. Three-day optimized kB^{-1} values are represented as the grey points, while the black line indicates the smoothed time series described in Section 2.4. Solid green curves indicate PhenoCam-derived G_{CC} and the vertical dashed lines indicate PhenoCam transition dates for green-up. The numbers printed next to each green-up line indicates the day-of-year of green-up. (For interpretation of the references to color in this figure legend, the reader is referred to the web version of this article.)

3.3. R_{ah} seasonality in croplands

There were relatively unique patterns at several of the cropland sites in our analysis, compared to other sites. Specifically, a significant proportion of the variation in R_{ah} was attributable to R_{am}, contrasting with results at most other sites (Fig. 4). R_{am} exhibited significant influence at

the Nebraska corn and soybean agricultural sites (US-Ne1, US-Ne2, and US-Ne3). Our attribution analysis indicated R_{am} explained a significant part of the total variance in R_{ah}, with R_{am} explaining 37% and 52% of the variability in R_{ah} for corn and soybean, respectively, compared to R_{bh} which explained 47% and 48%. This similarity can be visualized in Fig. 2, as both R_{ah} and R_{am} closely tracked each other immediately after
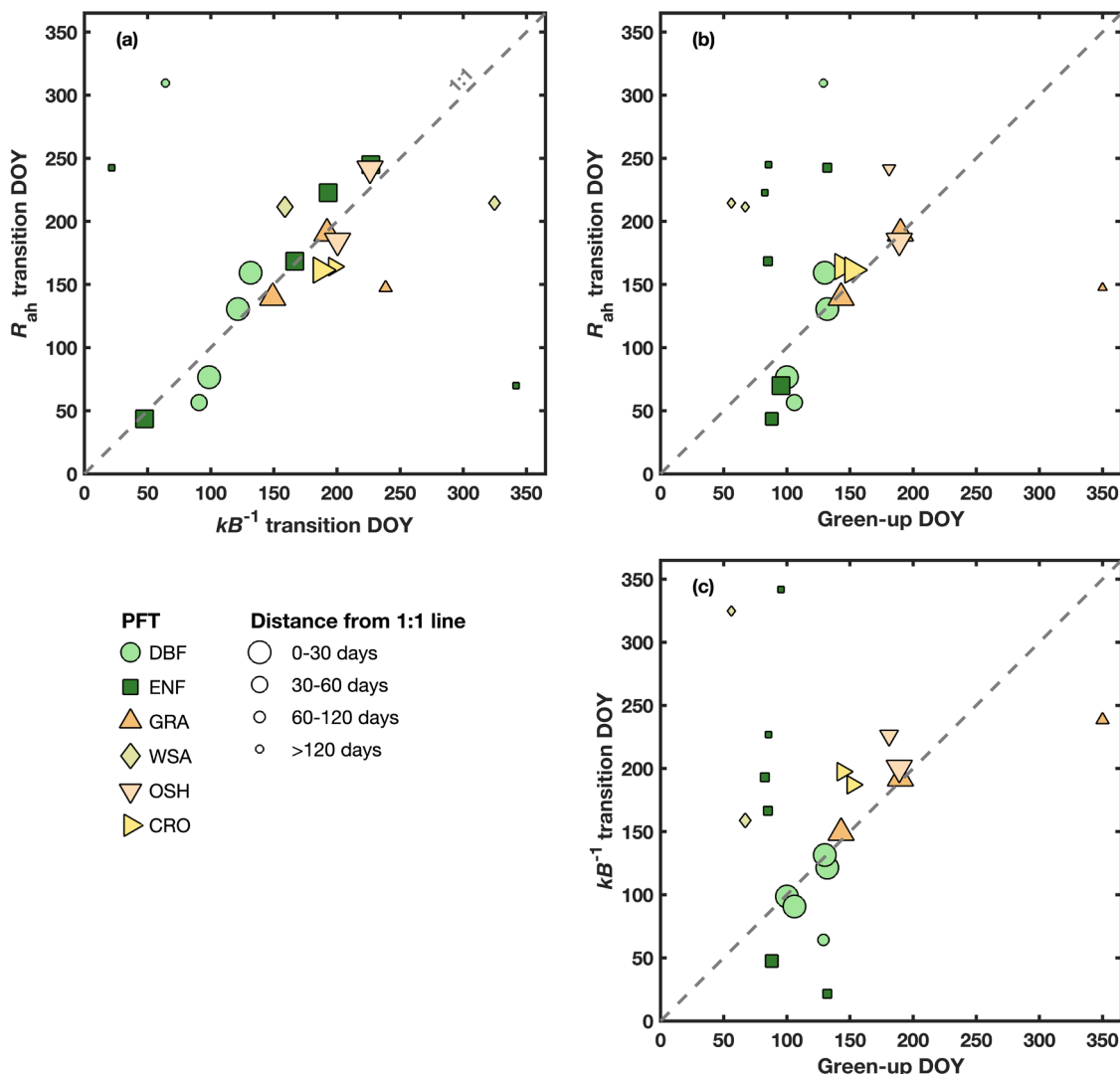
Fig. 7. Comparison of transition dates for R_{ah}, kB^{-1}, and green-up. Plot symbols and colors indicate different PFTs, while the size of the plot points is inversely proportional to the distance from the 1:1 line. Transition dates for R_{ah} and kB^{-1} are equated to the end points for the empirical distribution of the timing of maximum values for each variable (e.g., see Figs. 3 and 5).

green-up in both corn and soybean sites. Seasonal patterns in R_{bh} and kB^{-1} also differed notably compared to deciduous forest and grassland sites; R_{bh} and kB^{-1} in cropland sites increased immediately after green-up, followed by a sudden decrease after canopy greenness reached its seasonal maximum (Figs. 2 and 6).

Strong seasonal patterns in R_{ah} were also observed at weekly time-scales at the alfalfa (*Medicago sativa* L.) sites in the Sacramento–San Joaquin River Delta in central California (US-Bi1 and US-Tw3), with R_{ah} and kB^{-1} decreasing as z_{0m} and canopy greenness increased (Figs. 9 and S7). Alfalfa harvesting takes place 5-7 times per year during the spring and summer (Hemes et al., 2019). At these two sites, we observed distinct seasonal patterns in R_{ah} responding to changes in aerodynamic canopy height (h_a), canopy greenness, and kB^{-1} (Fig. 9 and S7). At US-Bi1, changes in z_{0m} ranged from 0.02 to 0.06 m, closely tracking canopy greenness, and R_{ah} and kB^{-1} inversely tracked these changes in h_a and greenness. Similar patterns were found at US-Tw3 (Fig. S7). The data at these sites highlight three key patterns. First, kB^{-1} was the main driver of R_{ah}. Second, maximum values in R_{ah} and kB^{-1} occurred when canopy greenness and z_{0m} were at a minimum, shortly after a harvesting event. Finally, there was little-to-no change in R_{am} accompanying these patterns in R_{ah}. These results were comparable to the patterns observed in deciduous broadleaf, grassland, and shrubland sites; maximum and

minimum values of R_{ah} and kB^{-1} occurred during dormant and growing periods, respectively.

3.4. Implications for understanding seasonal changes in aerodynamic resistance

At many sites, we found evidence that kB^{-1} differs between the non-growing season and growing season, indicated by the clear bifurcation in kB^{-1} with higher values occurring during the non-growing season and lower values occurring during the growing season (Fig. 10). To understand how this seasonal variation in kB^{-1} may influence predictions of H when compared to the assumption of static kB^{-1} (i.e., $kB^{-1} = 0$ or $kB^{-1} = c$), we estimated the full annual pattern of relative differences between estimated and measured H (i.e., $\hat{H}/H$) at a 3-day timestep. We found that estimates of H were quite sensitive to $kB^{-1} = 0$ or $kB^{-1} = c$; at many sites, we found that the highest relative differences generally occurred during the nongrowing season and under the assumption $kB^{-1} = 0$ (Fig. 11). For example, at US-MMS, $\hat{H}/H$ was approximately 300% right before green-up, indicating that assuming $kB^{-1} = 0$ will produced large biases (Fig. 11). At the arid US-Ses shrubland site, the highest values of $\hat{H}/H$ ($> 400\%$) occurred immediately prior to green-up (Fig. 11). We found similar seasonal patterns of $\hat{H}/H$ by assuming
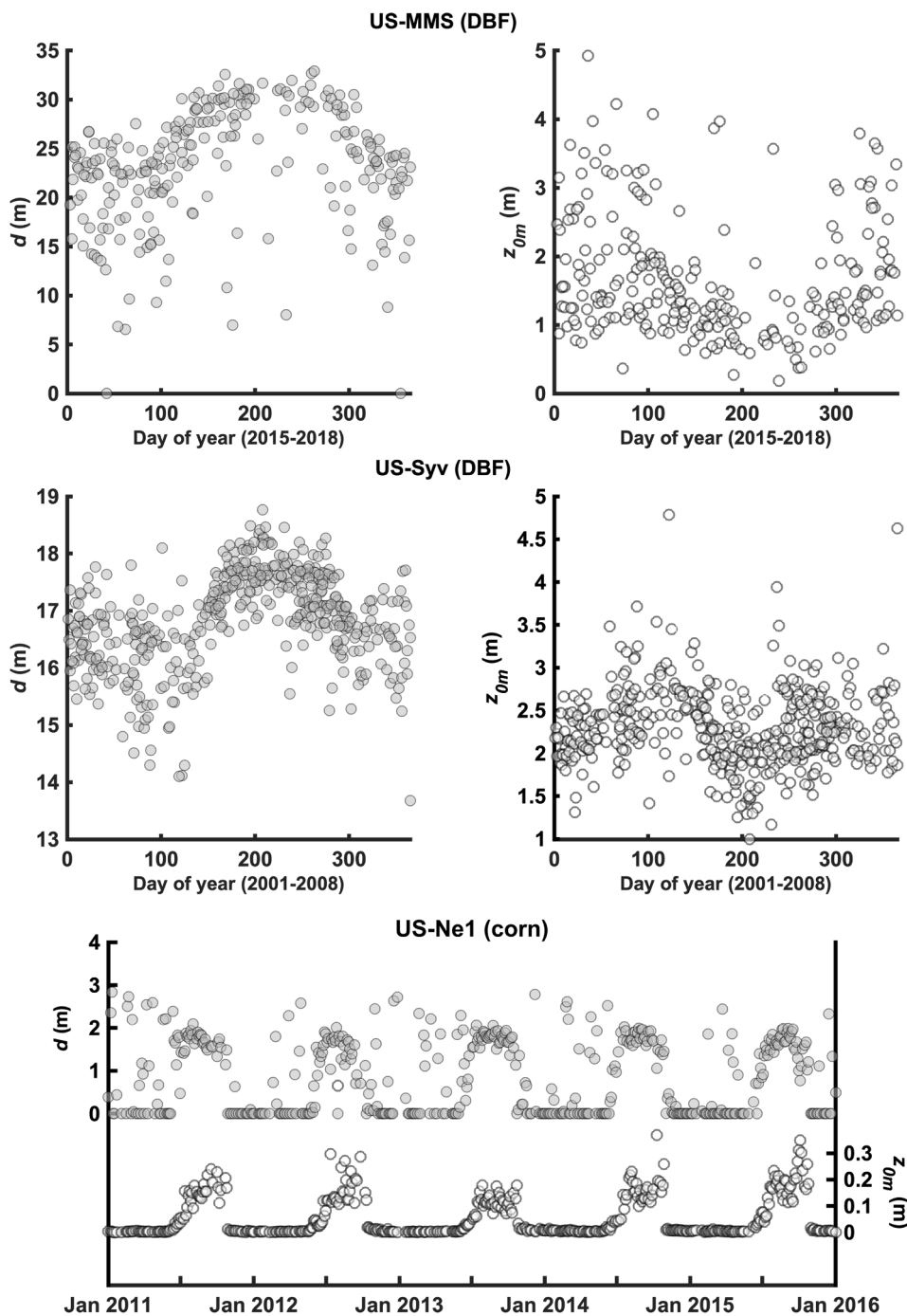
Fig. 8. Changes in d and z_{0m} estimated from wind-profile data.

kB^{-1} is constant for each PFT (i.e., $kB^{-1} = c$), although the magnitude of $\hat{H}/H$ was considerably reduced relative to $kB^{-1} = 0$ (Fig. 11). Furthermore, the seasonal patterns in $\hat{H}/H$ observed at many sites were similar to the seasonal patterns in R_{ah} (Fig. 2). In summary, these results indicated that accounting for seasonal changes in kB^{-1} is critical for significantly reducing biases and errors when predicting H using a "big leaf" approach.

4. Discussion

Using 190 site-years of data from the AmeriFlux and PhenoCam networks, our findings highlight how aerodynamic resistance to heat transfer (R_{ah}) exhibits distinct seasonal patterns among multiple plant-functional types (PFTs) and climate regimes, and how vegetation phenology may play a role governing this seasonality in certain PFTs. Specifically, PFTs that exhibit the strongest seasonal changes in canopy structure also consistently displayed strong seasonality in R_{ah}, and the timing of the seasonal patterns in R_{ah} closely track phenological start-of-season green-up at most of these sites. Incorporating these seasonal patterns of R_{ah}, as well as potential linkages to spring phenology, is important for improving model-based predictions of sensible heat fluxes, and thus our understanding of how seasonal changes in the land surface more broadly impact atmospheric dynamics such as boundary layer height, vertical temperature profiles, and near-surface micro-climate.

Fig. 9. Growing season patterns in z_{0m} (i.e., $0.1h_a$), G_{CC}, R_{am}, R_{bh}, R_{ah}, and kB^{-1} for an agricultural site (US-Bi1) for 2017. Images are from the PhenoCam site bouldinalfalfa at midday. Due to the short time period, these data are daily (individual p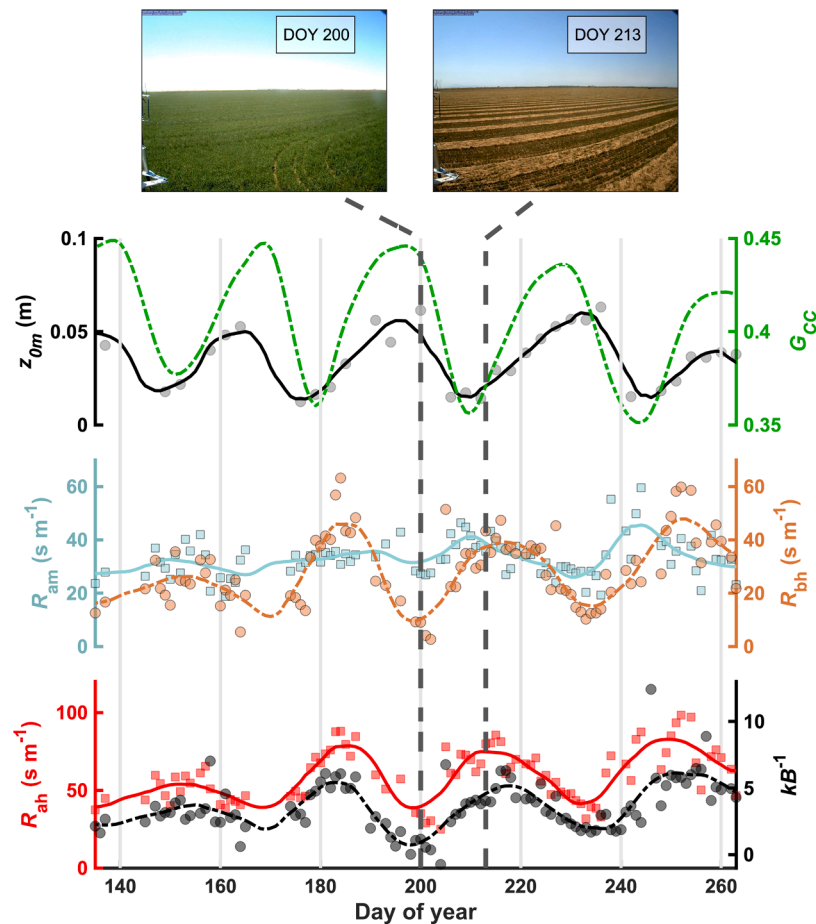oints) and smoothed using a loess. Solid and dashed lines represent the smoothed values for the left and right y axes, respectively.

4.1. How does aerodynamic resistance change seasonally?

The aerodynamic resistance to heat transfer (R_{ah}) comprises two additive resistance terms ($R_{ah} = R_{am} + R_{bh}$, Eq. (2)), and our findings provide evidence that for most sites excess resistance to heat transfer (R_{bh}) is a significantly stronger control over seasonal patterns of R_{ah}, relative to the resistance to momentum transfer (R_{am}) (Figs. 2–5). Recall that excess resistance (R_{bh}) accounts for differences between the roughness lengths for momentum (z_{0m}) and heat (z_{0h}) through the kB^{-1} parameter (i.e., $k \cdot R_{bh} \cdot u_* = \ln(z_{0m}/z_{0h}) = kB^{-1}$, Eq. (7)). In this study, we found that the seasonality (Figs. 2, 3, 5, 7a) and total variance (Fig. 4) in R_{ah} is best explained by R_{bh} and kB^{-1}. Taken together, these multiple relationships linking kB^{-1} to R_{ah} through R_{bh} imply changes in surface roughness (i.e., through z_{0m} or z_{0h}) are a key factor determining seasonal patterns in R_{ah}.

At most deciduous broadleaf, grassland, and shrubland sites, kB^{-1} decreases during start-of-season phenological transitions, implying the potential for a direct causal linkage between phenology and seasonal changes in kB^{-1} (Figs. 6, 7 and 10). Decreasing kB^{-1} in response to increasing LAI has been identified in other studies. For example, kB^{-1} is commonly modeled as a function of LAI (Brutsaert, 1979; Hu et al., 2020; Kubota and Sugita, 1994; Yang and Friedl, 2003). This modeling captures decreases of kB^{-1} in response to increasing LAI and provides accurate estimates of H as well (Qualls and Brutsaert, 1996). Decreasing kB^{-1} after green-up must be related to either z_{0m} or z_{0h} (Eq. (6)). Here, we conclude z_{0h} is more influential than z_{0m} in most cases. Specifically, we posit shifts to higher z_{0h} (lower kB^{-1}) during start-of-season green-up are due to decreases in the fractional coverage of understory and bare

soil. Landscapes dominated by bare soil or sparse vegetation exhibit z_{0h} heights effectively at the soil surface, especially during warm and dry meteorological conditions where the soil is acting the primary source of heat (Verhoef et al., 1997; Yang et al., 2008). A theoretical addition of taller un-foliated roughness elements to a landscape would increase z_{0m}, while z_{0h} would remain unchanged due to surface temperature of the understory exceeding that of the canopy temperature (Brutsaert and Sugita, 1996). During phenological transitions, such as leaf emergence in temperate deciduous forests, the canopy fills in, the coverage of bare soil and understory decreases, and transpiration increases cooling of the surface (Verhoef et al., 1997), together leading to increases in z_{0h} and lowering kB^{-1}. Similar behavior of kB^{-1} is found between PFTs that have dense and sparse canopies. Permeable-rough surfaces (e.g., deciduous broadleaf or agriculture sties) have kB^{-1} values lower than bluff-rough surfaces (e.g., shrubland sites) (Brutsaert, 1982; Rigden et al., 2018). These bluff-rough surfaces, generally occurring at more arid sites, have higher proportions of land cover dominated by bare soil (Fig. S3).

While changes in z_{0m}, as well as z_{0h}, may also play a role in altering kB^{-1}, our results imply that observed changes in z_{0m} are not driving seasonal decreases in kB^{-1}. Specifically, we found that z_{0m} generally increases during the growing season, indicated by increasing aerodynamic canopy height (h_a; Fig. S4) or wind-profile data (Fig. 8). All other factors being equal, increasing z_{0m} by itself would lead to higher kB^{-1}; however, we found that kB^{-1} decreases after green-up (Figs. 5, 6, 9, and 10). Therefore, we infer that increases in z_{0h} offset increasing z_{0m}, thereby leading to decreases in kB^{-1} (e.g., Fig. 1) and implying z_{0h} is the more important control over kB^{-1}. Patterns observed at an alfalfa agricultural site (US-Bi1, Fig. 9) capture this dynamic. Significant decreases
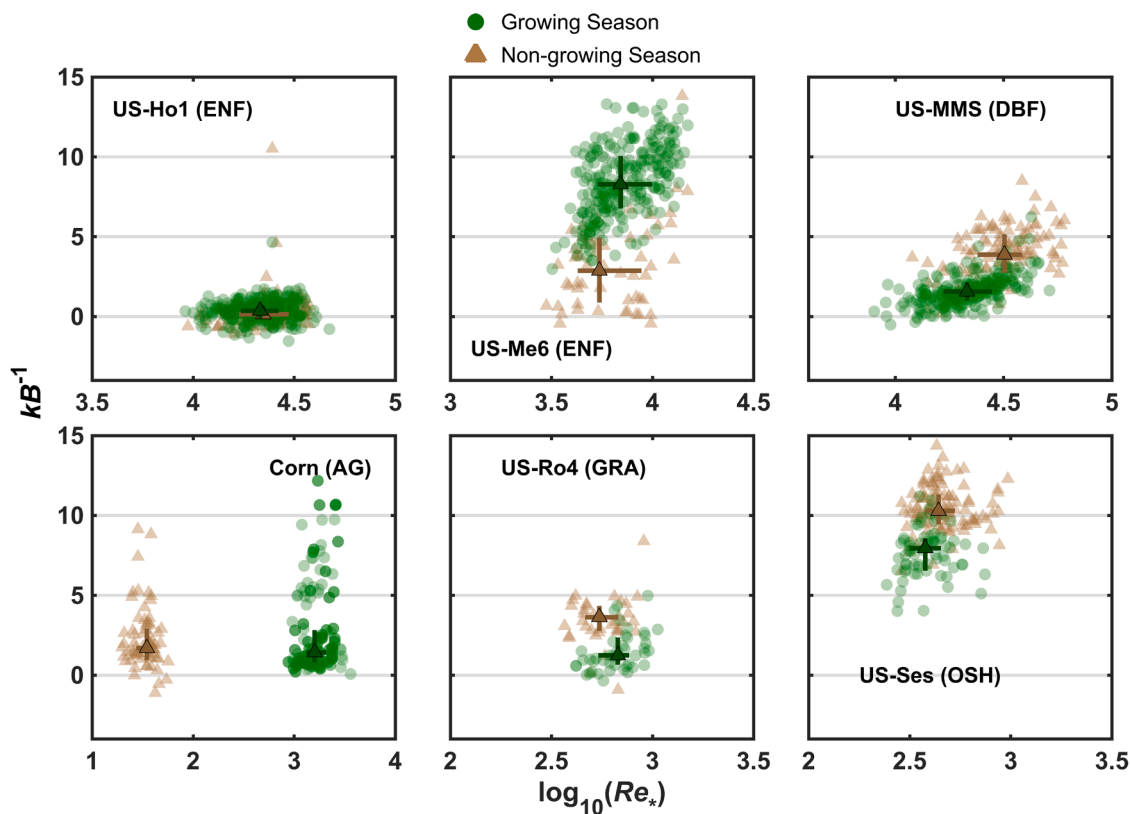
Fig. 10. Relationships between kB^{-1} and the Reynolds roughness number (Re_*) for different phenology phases (non-growing and growing season) at six example sites. The darker plot points and confidence bounds represent the median and inter-quartile range of the distributions along each axis.

in z_{0m} after a harvesting event by itself should lead to decreasing kB^{-1}. However, we found kB^{-1} increases after harvesting events, likely due to significant decrease in z_{0h} relative to z_{0m}. Increases in z_{0m} after green-up, while common, are not ubiquitous. Decreases in z_{0m} can also occur. Specifically, functions relating z_{0m} to the plant area index (i.e., PAI) exhibit non-monotonic relationship and higher leaf area and foliage density at the top of the canopy can act as a smooth surface (Blanken and Black, 2004; Shaw and Pereira, 1982). While we see such decreases in z_{0m} at US-MMS, US-Syv, and US-NR1 (Figs. 8 and S4), this likely does not outweigh the importance of z_{0h} given its strong influence at other sites.

While z_{0h} may have more control over seasonal changes in R_{ah} relative to z_{0m}, this is partially due to z_{0m} simply not changing as much relative to z_{0h} between the non-growing and growing seasons, as the physical structure of the canopy generally remains in place even if it is defoliated (Nakai et al., 2008). Using the corn and soybean sites, we can investigate and better understand the influence of z_{0m} in a system where the landscape transforms from bare soil to a full canopy within a season. Here, we found patterns in R_{am} closely tracking R_{ah} (Fig. 2), and R_{am} explains significantly more of the observed variance in R_{ah} compared to other sites (Fig. 4). This increased importance in R_{am} is due to significant increases in z_{0m} as the crops increase in height (Figs. 2 and 8) and the subsequent effect on the log-wind profile Eqn (13).

Phenology does not have the same level of control over R_{ah} in evergreen-needleleaf sites (Figs. 2, 3 and 5). This is not surprising, given that our evergreen-needleleaf sites exhibit only minor leaf turnover each season. Where we did observe seasonal changes in R_{ah} (e.g., US-Me6), these changes are also associated with changes in R_{bh} and kB^{-1}, comparable to other PFTs. Therefore, changes in R_{ah} in evergreen-needleleaf sites are not driven by changing leaf area and the fractional cover of the forest canopy, but likely by two other interacting factors. First, increasing solar radiation and surface heating during the course of the growing season alters the temperature source height (z_{0h}), thereby altering R_{ah} through kB^{-1}, comparable to diurnal changes in kB^{-1}

tracking solar radiation (Fig. 1) (Lhomme et al., 1997; Yang et al., 2008). Second, these impacts of seasonal changes in solar radiation on kB^{-1} only occur at more arid sites with taller vegetation, compared to shrublands or grasslands, and that likely have lower stand density (i.e., US-Me2, US-Me6, and US-Mpj; Figs. 2 and S3). The higher exposure of the understory or bare soil, compared to the more closed canopy sites (i. e., CA-TP4, US-Ho1, US-NR1), exacerbates the effects these changing environmental conditions have on kB^{-1}. Finally, it should be noted that phenology may still play an important role in controlling seasonal patterns of kB^{-1} at lower density evergreen-needleleaf sites through the phenology of understory vegetation. However, the greenness index from PhenoCam for these sites is only derived for the canopy and does not capture the understory phenology.

From this analysis we conclude that phenology can be a key driver over observed seasonal shifts in kB^{-1} in some ecosystems, which subsequently influences R_{ah} and predictions of H. However, the full seasonal trajectory of kB^{-1} is not explained by phenology alone; across the sites we considered, significant variations in R_{bh} and kB^{-1} occurred well before and after phenological transitions (Figs. 2 and 6). For example, at a semi-arid grassland site in southern Arizona (US-Wkg), we observed distinct increases in kB^{-1} beginning in January of each year, which continued throughout the dormant season prior to green-up (Fig. 6). These shifts in kB^{-1} occurred well after senescence and before spring green-up, and such shifts are likely influenced by other environmental or meteorological factors, including evapotranspiration, net radiation, wind speed, and surface temperature (e.g., Blyth and Dolman, 1995; Lhomme et al., 1997). As a brief supplementary analysis, we conducted a multiple linear regression at US-Wkg that related kB^{-1} to a list of meteorological factors: R_n, surface temperature (T_s), latent heat flux, soil water content, wind speed, and cumulative 10-day precipitation. We found that T_s emerged as the most important among these variables at seasonal time scales ($p < 0.001$ and partial correlation = 0.437, Table S2), having a strong positive relationship with kB^{-1} (Fig. S8). This
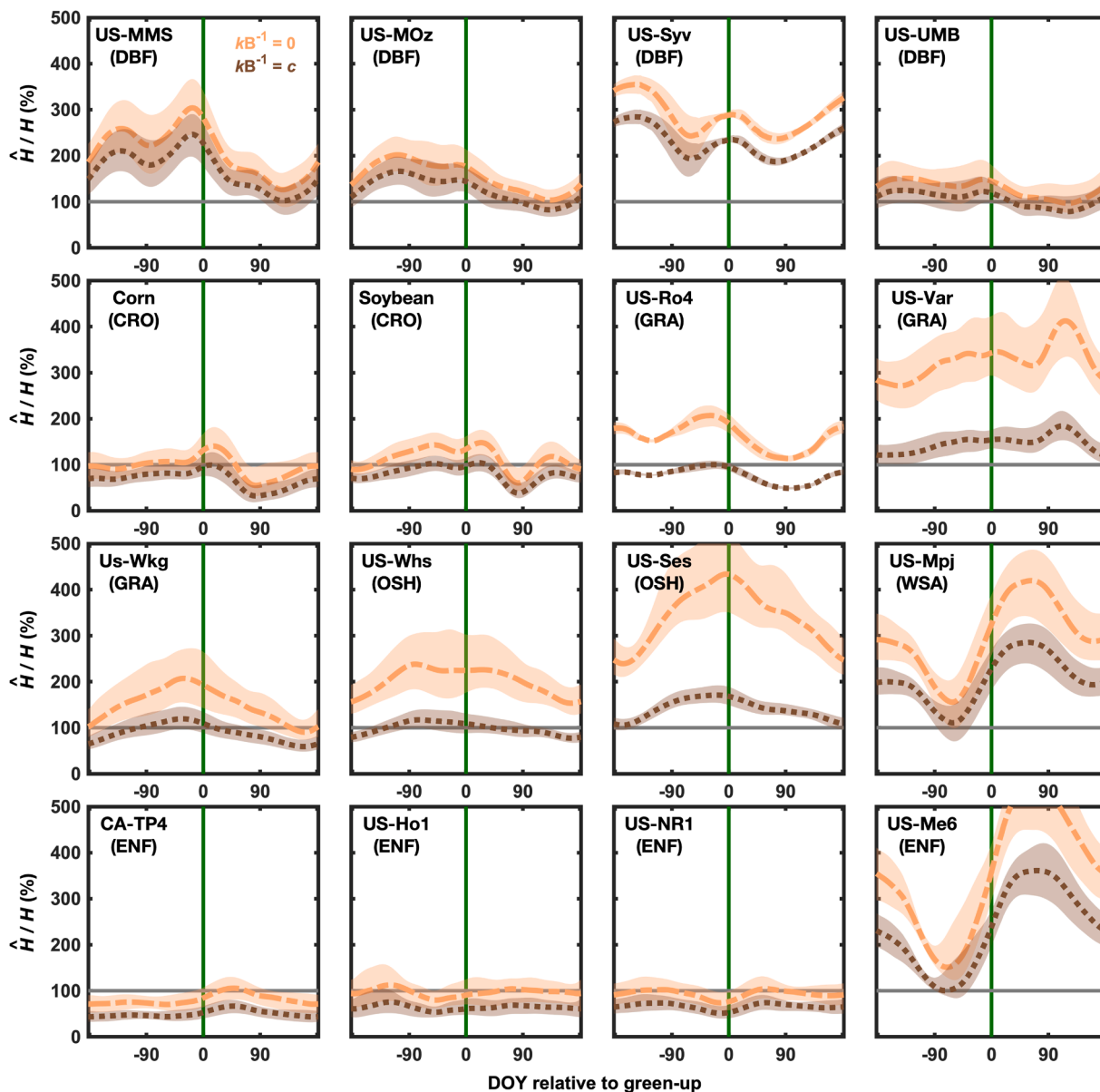
Fig. 11. Seasonal signals in relative differences between measured and estimated sensible heat flux ($\hat{H}/H$) for different sites depending on whether kB^{-1} is assumed equal to 0 or a constant (i.e., $kB^{-1} = 0$ or $kB^{-1} = c$). Lines and confidence bounds are the median and interquartile range across all years.

influence of T_s is likely due to progressively warmer soil conditions that occur from January-June under increasing R_n, with the soil thereby acting as the primary source of heat exchange, relative to the canopy, and resulting in z_{0h} to be at the height of the soil surface. As monsoonal precipitation begins in late-June or July and green-up occurs, the soil temperature shifts and begins to cool and is therefore less sensitive to continued increases in R_n that occur during the remainder of the summer. While this analysis is admittedly brief, it does indicate that there are other potential drivers of seasonality in kB^{-1}. In general, quantifying the influence of these factors on kB^{-1} – as well as how they interact with each other and phenology – is crucial for developing accurate models of kB^{-1}.

4.2. How does changing aerodynamic resistance influence predictions of H?

Substantial differences between estimated ($\hat{H}$) and measured H occurred when kB^{-1} is assumed constant or equal to 0 (Fig. 11). These results have important implications for modeling of the land-surface

energy balance using "big leaf" energy balance equations (e.g., Eq. (1)). First, simplified assumptions of a static kB^{-1} (i.e., $kB^{-1} = 0$ or kB^{-1} is constant) are insufficient to accurately model the complete seasonal trajectory of H. Assuming $z_{0m} = z_{0h}$ (i.e., $kB^{-1} = 0$) appears to be invalid for vegetated surfaces, a result agreeing well with the literature (Yang et al., 2008). Similarly, assuming a constant value for each PFT, while helping to reduce biases (i.e., $\hat{H}/H$) relative to the assumption $kB^{-1} = 0$, still resulted in significant seasonal deviations from measured H at many sites. These results demonstrate that including a time-varying estimate of kB^{-1} that accounts for changes can eliminate seasonal patterns in $\hat{H}/H$ compared to assuming $kB^{-1} = 0$ or $kB^{-1} = c$, implying that anticipating how and why surface roughness changes is important for understanding seasonal dynamics in land-atmosphere interactions (Blythe and Dolman, 1994; Kustas et al., 1989).

4.3. Implications and directions for future work

The sensitivity of H to seasonal variations in kB^{-1} is unexpected when compared to inferences from past studies. Increasing z_{0m} under

land-cover shifts from grasslands to aerodynamically rougher forests leads to increased turbulence and decreasing resistance, subsequently impacting surface temperature (Burakowski et al., 2018; Lee et al., 2011). Such mechanisms have been suggested to occur during phenological transitions; increases in z_{0m} during green-up could decrease aerodynamic resistance to momentum transfer (Peñuelas et al., 2009). Conversely, phenology may only play a minor role controlling aerodynamic resistance. For example, in deciduous broadleaf forests, observed increases in R_{ah} during phenological transitions have been attributed to decreasing synoptic-scale wind speed, and not z_{0m} (Moon et al., 2020). Overall, our findings provide important new insight into the role of seasonally changing surface roughness, which in many cases appears to be associated with phenology, as a control on H. Perhaps more consequentially, the significant seasonal biases observed under the assumption of constant kB^{-1} implies the behavior for both z_{0m} and z_{0h} represents a key source of uncertainty for modeling land-atmosphere interactions.

Resolving uncertainty in the behavior of z_{0m} and z_{0h} at seasonal time scales is not only important for model improvement, but also critical for understanding how seasonal changes in H may impact atmospheric dynamics, such as boundary layer height, temperature profiles, and micro-climate (Helbig et al., 2020). For example, due to the exponential nature of kB^{-1} (Eq. (6)), small increases in z_{0h} would reduce R_{ah}, leading to increased H and potentially decreasing aerodynamic surface temperature and near-surface air temperature (Novick and Katul, 2020). Understanding such dynamics will likely be important for anticipating ecosystem impacts as phenology responds to a changing climate (Richardson et al., 2013). To reduce this uncertainty, developing prognostic models of kB^{-1} as a function of different environmental factors – including phenology – is a key next step. Other studies have modeled differences in kB^{-1} among different PFTs, for example as a function of u_* or Re_* (e.g., Rigden et al., 2018). Expanding on such models to capture the seasonal shifts and bifurcation of kB^{-1} would lead to a stronger understanding of how the horizontal and vertical structure of surface roughness elements impacts H (Garratt and Hicks, 1973; Maurer et al., 2013). Finally, while more complex land-surface models such as CLM or a multi-layer approach do not rely on kB^{-1}, our work motivates the need for investigations into how seasonal changes in land-surface properties might impact predictions from these systems-based models.

Conclusions

Through a continental-scale synthesis integrating AmeriFlux and PhenoCam data and applying Monin–Obukhov similarity theory, we find that seasonal variability in aerodynamic resistance to heat transfer is pervasive across a range of ecosystems. We found evidence that the mechanisms underlying this variation in aerodynamic resistance are likely linked to vegetation phenology in deciduous broadleaf forests, grasslands, croplands, and shrublands. Specifically, shifts to a larger leaf area led to z_{0h} increases during green-up, leading to decreases in kB^{-1} and in the overall total aerodynamic resistance to heat transfer. By comparison, the role of changing surface roughness to momentum transfer (z_{0m}) appeared to be minimal compared to z_{0h}. The total impact of seasonal variation in kB^{-1} on model-based estimates of sensible-heat flux is important; large biases in ($\hat{H}/H$) occurred when assuming kB^{-1} is constant. Predicting the full seasonal trajectory of sensible heat flux using simple one-layer land-surface energy balance models requires prognostic models and parametrizations that account for seasonal changes in kB^{-1} in response to phenology and other environmental and meteorological factors. In conclusion, we found evidence vegetation phenology can influence surface-roughness at relatively fine temporal scales, directly impacting seasonal variability in aerodynamic resistance to heat transfer across a range of North American ecosystems. Because this variation in aerodynamic resistance also influences the land-surface energy balance, our findings provide insight into how land-atmosphere interactions operate at seasonal time scales.

References

Agostinelli, C. and Lund, U., 2017. R package 'circular': Circular Statistics (version 0.4-93). https://r-forge.r-project.org/projects/circular/.

Anderson-Teixeira, K.J., Delong, J.P., Fox, A.M., Brese, D.A., Litvak, M.E., 2011. Differential responses of production and respiration to temperature and moisture drive the carbon balance across a climatic gradient in New Mexico. Glob. Change Biol. 17 (1), 410–424. https://doi.org/10.1111/j.1365-2486.2010.02269.x.

Baldocchi, D., Ma, S.Y., 2013. How will land use affect air temperature in the surface boundary layer? Lessons learned from a comparative study on the energy balance of an Oak Savanna and annual grassland in California, USA. Tellus Ser. B-Chem. Phys. Meteorol. 65 https://doi.org/10.3402/tellusb.v65i0.19994.

Betts, A.K., 2004. Understanding hydrometeorology using global models. Bull. Am. Meteorol. Soc. 85 (11) https://doi.org/10.1175/Bams-85-11-1673, 1673-+.

Blanken, P.D., Black, T.A., 2004. The canopy conductance of a boreal aspen forest, Prince Albert National Park, Canada. Hydrol. Process. 18 (9), 1561–1578. https://doi.org/10.1002/hyp.1406.

Blyth, E.M., Dolman, A.J., 1995. The roughness length for heat of sparse vegetation. J. Appl. Meteorol. 34 (2), 583–585. https://doi.org/10.1175/1520-0450-34.2.583.

Bonan, G., 2016. Ecological Climatology: Concepts and Applications. Cambridge University Press, New York, p. 679.

Bowling, D.R., et al., 2018. Limitations to winter and spring photosynthesis of a Rocky Mountain subalpine forest. Agr. For. Meteorol. 252, 241–255. https://doi.org/10.1016/j.agrformet.2018.01.025.

Brutsaert, W., 1979. Heat and mass-transfer to and from surfaces with dense vegetation or similar permeable roughness. Bound. Layer Meteorol. 16 (3), 365–388. https://doi.org/10.1007/Bf02220492.

Brutsaert, W., 1982. Evaporation into the Atmosphere: Theory, History, and Applications. Springer, Netherlands, p. 299 pp.

Brutsaert, W., Sugita, M., 1996. Sensible heat transfer parameterization for surfaces with anisothermal dense vegetation. J. Atmosp. Sci. 53 (2), 209–216. https://doi.org/10.1175/1520-0469(1996)053<0209:Shtpfs>2.0.Co;2.

Burakowski, E., et al., 2018. The role of surface roughness, albedo, and Bowen ratio on ecosystem energy balance in the Eastern United States. Agr. For. Meteorol. 249, 367–376. https://doi.org/10.1016/j.agrformet.2017.11.030.

Burns, S.P., Blanken, P.D., Turnipseed, A.A., Hu, J., Monson, R.K., 2015. The influence of warm-season precipitation on the diel cycle of the surface energy balance and carbon dioxide at a Colorado subalpine forest site. Biogeosciences 12 (23), 7349–7377. https://doi.org/10.5194/bg-12-7349-2015.

Businger, J.A., Wyngaard, J.C., Izumi, Y., Bradley, E.F., 1971. Flux-profile relationships in the atmospheric surface layer. J. Atmos. Sci. 28 (2), 181–189 https://doi.org/10.1175/1520-0469(1971)028%3C0181:FPRITA%3E2.0.CO;2.

Campbell, G.S., Norman, J.M., 1998. An Introduction to Environmental Biophysics. Springer, New York, p. 286.

Chu, H.S., et al., 2018. Temporal dynamics of aerodynamic canopy height derived from eddy covariance momentum flux data across North American flux networks. Geophys. Res. Lett. 45 (17), 9275–9287. https://doi.org/10.1029/2018gl079306.

Cook, B.D., et al., 2004. Carbon exchange and venting anomalies in an upland deciduous forest in northern Wisconsin, USA. Agr. For. Meteorol. 126 (3-4), 271–295. https://doi.org/10.1016/j.agrformet.2004.06.008.

Desai, A.R., Bolstad, P.V., Cook, B.D., Davis, K.J., Carey, E.V., 2005. Comparing net ecosystem exchange of carbon dioxide between an old-growth and mature forest in the upper Midwest, USA. Agr. For. Meteorol. 128 (1-2), 33–55. https://doi.org/10.1016/j.agrformet.2004.09.005.

Dolman, A.J., 1986. Estimates of roughness length and zero plane displacement for a foliated and non-foliated oak canopy. Agr. For. Meteorol. 36 (3), 241–248. https://doi.org/10.1016/0168-1923(86)90038-9.

Dragoni, D., et al., 2011. Evidence of increased net ecosystem productivity associated with a longer vegetated season in a deciduous forest in south-central Indiana, USA. Glob. Change Biol. 17 (2), 886–897. https://doi.org/10.1111/j.1365-2486.2010.02281.x.

Dyer, A.J., Hicks, B.B., 1970. Flux-gradient relationships in constant flux layer. Q. J. R. Meteorolog. Soc. 96 (410), 715-+. https://doi.org/10.1002/qj.49709641012.

Fitzjarrald, D.R., Acevedo, O.C., Moore, K.E., 2001. Climatic consequences of leaf presence in the eastern United States. J. Clim. 14 (4), 598–614. https://doi.org/10.1175/1520-0442(2001)014<0598:Ccolpi>2.0.Co;2.

Garratt, J.R., Francey, R.J., 1978. Bulk characteristics of heat transfer in the unstable, baroclinic atmospheric boundary layer. Bound. Layer Meteorol. 15 (4), 399–421. https://doi.org/10.1007/BF00120603.

Garratt, J.R., Hicks, B.B., 1973. Momentum, heat and water-vapor transfer to and from natural and artificial surfaces. Q. J. R. Meteorol. Soc. 99 (422), 680–687. https://doi.org/10.1256/smsqj.42208.

Gough, C.M., et al., 2013. Sustained carbon uptake and storage following moderate disturbance in a Great Lakes forest. Ecol. Appl. 23 (5), 1202–1215. https://doi.org/10.1890/12-1554.1.

Gu, L.H., et al., 2016. Testing a land model in ecosystem functional space via a comparison of observed and modeled ecosystem flux responses to precipitation regimes and associated stresses in a Central US forest. J. Geophys. Res.-Biogeosci. 121 (7), 1884–1902. https://doi.org/10.1002/2015jg003302.

Hagen, S.C., et al., 2006. Statistical uncertainty of eddy flux-based estimates of gross ecosystem carbon exchange at Howland Forest, Maine. J. Geophys. Res.-Atmosp. 111 (D8) https://doi.org/10.1029/2005jd006154.

Helbig, M. et al., 2020. Understanding land-atmosphere interactions through tower-based flux and continuous atmospheric boundary layer measurements [White paper]. https://ameriflux.lbl.gov/community/highlight/whitepaper-understanding-land-atmosphere-interactions-through-tower-based-flux-and-continuous-atmospheric-boundary-layer-measurements/.

Hemes, K.S., et al., 2019. Assessing the carbon and climate benefit of restoring degraded agricultural peat soils to managed wetlands. Agr. For. Meteorol. 268, 202–214. https://doi.org/10.1016/j.agrformet.2019.01.017.

Hollinger, D.Y., et al., 1999. Seasonal patterns and environmental control of carbon dioxide and water vapour exchange in an ecotonal boreal forest. Glob. Change Biol. 5 (8), 891–902. https://doi.org/10.1046/j.1365-2486.1999.00281.x.

Hollinger, D.Y., Richardson, A.D., 2005. Uncertainty in eddy covariance measurements and its application to physiological models. Tree Physiol. 25 (7), 873–885. https://doi.org/10.1093/treephys/25.7.873.

Hu, X., Shi, L., Lin, L., Magliulo, V., 2020. Improving surface roughness lengths estimation using machine learning algorithms. Agr. For. Meteorol. 287, 107956 https://doi.org/10.1016/j.agrformet.2020.107956.

Jenkins, J.P., et al., 2007. Refining light-use efficiency calculations for a deciduous forest canopy using simultaneous tower-based carbon flux and radiometric measurements. Agr. For. Meteorol. 143 (1-2), 64–79. https://doi.org/10.1016/j.agrformet.2006.11.008.

Keenan, T.F., et al., 2014. Tracking forest phenology and seasonal physiology using digital repeat photography: a critical assessment. Ecol. Appl. 24 (6), 1478–1489. https://doi.org/10.1890/13-0652.1.

Knauer, J., El-Madany, T.S., Zaehle, S., Migliavacca, M., 2018. Bigleaf-An R package for the calculation of physical and physiological ecosystem properties from eddy covariance data. PLoS One 13 (8). https://doi.org/10.1371/journal.pone.0201114.

Kubota, A., Sugita, M., 1994. Radiometrically determined skin temperature and scalar roughness to estimate surface heat-flux. Part I: parameterization of radiometric scalar roughness. Bound. Layer Meteorol. 69 (4), 397–416. https://doi.org/10.1007/Bf00718127.

Kustas, W.P., et al., 1989. Determination of sensible heat-flux over sparse canopy using thermal infrared data. Agr. For. Meteorol. 44 (3-4), 197–216. https://doi.org/10.1016/0168-1923(89)90017-8.

Lawrence, D.M., Fisher, R.A., Koven, C.D., Oleson, K.W., Swenson, S.C., Bonan, G., et al., 2019. The Community Land Model version 5: Description of new features, benchmarking, and impact of forcing uncertainty. J. Ad. Model. Earth Sys. 11, 4245–4287. https://doi.org/10.1029/2018MS001583.

Lee, X., et al., 2011. Observed increase in local cooling effect of deforestation at higher latitudes. Nature 479 (7373), 384–387. https://doi.org/10.1038/nature10588.

Lhomme, J.P., Troufleau, D., Monteny, B., Chehbouni, A., Bauduin, S., 1997. Sensible heat flux and radiometric surface temperature over sparse Sahelian vegetation II. A model for the kB-1 parameter. J. Hydrol. 188 (1-4), 839–854. https://doi.org/10.1016/S0022-1694(96)03173-3.

Ma, S., Baldocchi, D., Wolf, S., Verfaillie, J., 2016. Slow ecosystem responses conditionally regulate annual carbon balance over 15 years in Californian oak-grass savanna. Agr. For. Meteorol. 228, 252–264. https://doi.org/10.1016/j.agrformet.2016.07.016.

Ma, S.Y., Baldocchi, D.D., Xu, L.K., Hehn, T., 2007. Inter-annual variability in carbon dioxide exchange of an oak/grass savanna and open grassland in California. Agr. For. Meteorol. 147 (3-4), 157–171. https://doi.org/10.1016/j.agrformet.2007.07.008.

Markland, T.C., 2019. Carbon balance and evapotranspiration rates of a restored prairie and a conventional corn/soybean rotation. University of Minnesota - Twin Cities, Minneapolis, MN (M.S. Thesis).

Massman, W.J., 1999. A model study of kB(H)(-1) for vegetated surfaces using 'localized near-field' Lagrangian theory. J. Hydrol. 223 (1-2), 27–43. https://doi.org/10.1016/S0022-1694(99)00104-3.

Maurer, K.D., Hardiman, B.S., Vogel, C.S., Bohrer, G., 2013. Canopy-structure effects on surface roughness parameters: observations in a Great Lakes mixed-deciduous forest. Agr. For. Meteorol. 177, 24–34. https://doi.org/10.1016/j.agrformet.2013.04.002.

Milliman, T., et al., 2019. PhenoCam Dataset v2.0: Digital camera imagery from the PhenoCam Network, 2000-2018. ORNL DAAC, Oak Ridge, TN, USA. https://doi.org/10.3334/ORNLDAAC/1689.

Monteith, J.L., Unsworth, M.H., 2008. Principles of Environmental Physics. Academic Press, Amsterdam, p. 440.

Moon, M., Li, D., Rigden, A.J., Friedl, M.A., 2020. Modification of surface energy balance during springtime: the relative importance of biophysical and meteorological changes. Agr. For. Meteorol. 284, 107905 https://doi.org/10.1016/j.agrformet.2020.107905.

Nakai, T., et al., 2008. Parameterisation of aerodynamic roughness over boreal, cool- and warm-temperate forests. Agr. For. Meteorol. 148 (12), 1916–1925. https://doi.org/10.1016/j.agrformet.2008.03.009.

Novick, K.A., et al., 2018. The AmeriFlux network: a coalition of the willing. Agr. For. Meteorol. 249, 444–456. https://doi.org/10.1016/j.agrformet.2017.10.009.

Novick, K.A., Katul, G.G., 2020. The duality of reforestation impacts on surface and air temperature. J. Geophys. Res.-Biogeosci. 125 (4) https://doi.org/10.1029/2019jg005543.

Oikawa, P.Y., et al., 2017. Revisiting the partitioning of net ecosystem exchange of CO_2 into photosynthesis and respiration with simultaneous flux measurements of (CO2)-C-13 and CO_2, soil respiration and a biophysical model. CANVEG. Agr. For. Meteorol. 234, 149–163. https://doi.org/10.1016/j.agrformet.2016.12.016.

Owen, P.R., Thomson, W.R., 1963. Heat transfer across rough surfaces. J. Fluid Mech. 15 (3), 321–334. https://doi.org/10.1017/S0022112063000288.

Papale, D., et al., 2006. Towards a standardized processing of Net Ecosystem Exchange measured with eddy covariance technique: algorithms and uncertainty estimation. Biogeosciences 3 (4), 571–583. https://doi.org/10.5194/bg-3-571-2006.

Peichl, M., Arain, M.A., Brodeur, J.J., 2010. Age effects on carbon fluxes in temperate pine forests. Agr. For. Meteorol. 150 (7-8), 1090–1101. https://doi.org/10.1016/j.agrformet.2010.04.008.

Pennypacker, S., Baldocchi, D., 2016. Seeing the fields and forests: Application of surface-layer theory and flux-tower data to calculating vegetation canopy height. Bound.-Layer Meteorol. 158 (2), 165–182. https://doi.org/10.1007/s10546-015-0090-0.

Peñuelas, J., Rutishauser, T., Filella, I., 2009. Phenology feedbacks on climate change. Science 324 (5929), 887–888. https://doi.org/10.1126/science.1173004.

Petrie, M.D., Collins, S.L., Swann, A.M., Ford, P.L., Litvak, M.E., 2015. Grassland to shrubland state transitions enhance carbon sequestration in the northern Chihuahuan Desert. Glob. Change Biol. 21 (3), 1226–1235. https://doi.org/10.1111/gcb.12743.

Pitman, A.J., 2003. The evolution of, and revolution in, land surface schemes designed for climate models. Int. J. Climatol. 23 (5), 479–510. https://doi.org/10.1002/joc.893.

Qualls, R.J., Brutsaert, W., 1996. Effect of vegetation density on the parameterization of scalar roughness to estimate spatially distributed sensible heat fluxes. Water Resour. Res. 32 (3), 645–652. https://doi.org/10.1029/95wr03097.

Raupach, M.R., 1994. Simplified expressions for vegetation roughness length and zero-plane displacement as functions of canopy height and area index. Bound. Layer Meteorol. 71 (1-2), 211–216. https://doi.org/10.1007/Bf00709229.

Raupach, M.R., Finnigan, J.J., 1988. Single-layer models of evaporation from plant canopies are incorrect but useful, whereas multilayer models are correct but useless: discuss. Aust. J. Plant Physiol. 15, 705–716. https://doi.org/10.1071/PP9880705.

Rice, J.A., 2007. Mathematical Statistics and Data Analysis. Duxbury Advanced Series. Thomson/Brooks/Cole, Belmont, CA.

Richardson, A.D., et al., 2012. Terrestrial biosphere models need better representation of vegetation phenology: results from the North American Carbon Program Site Synthesis. Glob. Change Biol. 18 (2), 566–584. https://doi.org/10.1111/j.1365-2486.2011.02562.x.

Richardson, A.D., Hollinger, D.Y., 2005. Statistical modeling of ecosystem respiration using eddy covariance data: maximum likelihood parameter estimation, and Monte Carlo simulation of model and parameter uncertainty, applied to three simple models. Agr. For. Meteorol. 131 (3-4), 191–208. https://doi.org/10.1016/j.agrformet.2005.05.008.

Richardson, A.D., et al., 2018. Tracking vegetation phenology across diverse North American biomes using PhenoCam imagery. Sci. Data 5, 180028. https://doi.org/10.1038/sdata.2018.28.

Richardson, A.D., et al., 2013. Climate change, phenology, and phenological control of vegetation feedbacks to the climate system. Agr. For. Meteorol. 169, 156–173. https://doi.org/10.1016/j.agrformet.2012.09.012.

Rigden, A., Li, D., Salvucci, G., 2018. Dependence of thermal roughness length on friction velocity across land cover types: a synthesis analysis using AmeriFlux data. Agr. For. Meteorol. 249, 512–519. https://doi.org/10.1016/j.agrformet.2017.06.003.

Roman, D.T., et al., 2015. The role of isohydric and anisohydric species in determining ecosystem-scale response to severe drought. Oecologia 179 (3), 641–654. https://doi.org/10.1007/s00442-015-3380-9.

Ruehr, N.K., Law, B.E., Quandt, D., Williams, M., 2014. Effects of heat and drought on carbon and water dynamics in a regenerating semi-arid pine forest: a combined

experimental and modeling approach. Biogeosciences 11 (15), 4139–4156. https://doi.org/10.5194/bg-11-4139-2014.

Sakai, R.K., 2000. Observational study of turbulent exchange between the surface and canopy layer over several forest types. State University of New York at Albany, Albany, NY, p. 4780. Ph.D. Thesis.

Schwartz, M.D., 1992. Phenology and springtime surface-layer change. Month. Weather Rev. 120 (11), 2570–2578. https://doi.org/10.1175/1520-0493(1992)120<2570:Passlc>2.0.Co;2.

Scott, R.L., Biederman, J.A., Hamerlynck, E.P., Barron-Gafford, G.A., 2015. The carbon balance pivot point of southwestern US semiarid ecosystems: insights from the 21st century drought. J. Geophys. Res.-Biogeosci. 120 (12), 2612–2624. https://doi.org/10.1002/2015jg003181.

Scott, R.L., Hamerlynck, E.P., Jenerette, G.D., Moran, M.S., Barron-Gafford, G.A., 2010. Carbon dioxide exchange in a semidesert grassland through drought-induced vegetation change. J. Geophys. Res.-Biogeosci. 115 https://doi.org/10.1029/2010jg001348.

Seyednasrollah, B., et al., 2019a. PhenoCam Dataset v2.0: Vegetation phenology from Digital Camera Imagery. ORNL DAAC, Oak Ridge, TN, USA. https://doi.org/10.3334/ORNLDAAC/1674, 2000-2018.

Seyednasrollah, B., et al., 2021. Seasonal variation in the canopy color of temperate evergreen conifer forests. New Phytol. 229 (5), 2586–2600. https://doi.org/10.1111/nph.17046.

Seyednasrollah, B., et al., 2019b. Tracking vegetation phenology across diverse biomes using Version 2.0 of the PhenoCam Dataset. Sci. Data. https://doi.org/10.1038/s41597-019-0270-8, 6.

Shaw, R.H., Pereira, A.R., 1982. Aerodynamic roughness of a plant canopy - a numerical experiment. Agric. Meteorol. 26 (1), 51–65. https://doi.org/10.1016/0002-1571(82)90057-7.

Sonnentag, O., et al., 2011. Tracking the structural and functional development of a perennial pepperweed (Lepidium latifolium L.) infestation using a multi-year archive of webcam imagery and eddy covariance measurements. Agr. For. Meteorol. 151 (7), 916–926. https://doi.org/10.1016/j.agrformet.2011.02.011.

Sonnentag, O., et al., 2012. Digital repeat photography for phenological research in forest ecosystems. Agr. For. Meteorol. 152, 159–177. https://doi.org/10.1016/j.agrformet.2011.09.009.

Sugita, M., Kubota, A., 1994. Radiometrically determined skin temperature and scalar roughness to estimate surface heat-flux. Part II: performance of parameterized scalar roughness for the determination of sensible heat. Bound. Layer Meteorol. 70 (1-2), 1–12. https://doi.org/10.1007/Bf00712520.

Suyker, A.E., Verma, S.B., 2010. Coupling of carbon dioxide and water vapor exchanges of irrigated and rainfed maize-soybean cropping systems and water productivity. Agr. For. Meteorol. 150 (4), 553–563. https://doi.org/10.1016/j.agrformet.2010.01.020.

Suyker, A.E., Verma, S.B., 2012. Gross primary production and ecosystem respiration of irrigated and rainfed maize-soybean cropping systems over 8 years. Agr. For. Meteorol. 165, 12–24. https://doi.org/10.1016/j.agrformet.2012.05.021.

Tao, Z. et al, 2013. Effect of land cover on atmospheric processes and air quality over the continental United States - a NASA Unified WRF (NU-WRF) model study. Atmosp. Chem. Phys. 13 (13), 6207–6226. https://doi.org/10.5194/acp-13-6207-2013.

Thom, A.S., 1972. Momentum, mass and heat-exchange of vegetation. Q. J. R. Meteorolog. Soc. 98 (415) https://doi.org/10.1256/smsqj.41509, 124-&.

Thomas, C.K., et al., 2009. Seasonal hydrology explains interannual and seasonal variation in carbon and water exchange in a semiarid mature ponderosa pine forest in central Oregon. J. Geophys. Res.-Biogeosci. 114 https://doi.org/10.1029/2009jg001010.

Verhoef, A., DeBruin, H.A.R., VandenHurk, B.J.J.M., 1997. Some practical notes on the parameter kB(-1) for sparse vegetation. J. Appl. Meteorol. 36 (5), 560–572. https://doi.org/10.1175/1520-0450(1997)036<0560:Spnotp>2.0.Co;2.

Verma, S., 1989. Aerodynamic resistances to transfers of heat, mass and momentum. In: Black, T., Spittlehouse, D., Novak, M., Price, D. (Eds.), Estimation of Areal Evapotranspiration. International Association of Hydrological Sciences, Vancouver, B.C., pp. 13–20

Wharton, S., Falk, M., Bible, K., Schroeder, M., Paw, K.T., 2012. Old-growth CO_2 flux measurements reveal high sensitivity to climate anomalies across seasonal, annual and decadal time scales. Agr. For. Meteorol. 161, 1–14. https://doi.org/10.1016/j.agrformet.2012.03.007.

Yang, K., Koike, T., Ishikawa, H., Kim, J., Li, X., Liu, H., Liu, S., Ma, Y., Wang, J., 2008. Turbulent flux transfer over bare-soil surfaces: characteristics and parameterization. J. Appl. Meteorol. Climatol. 47 (1), 276–290. https://doi.org/10.1175/2007jamc1547.1.

Yang, R.Q., Friedl, M.A., 2003. Determination of roughness lengths for heat and momentum over boreal forests. Bound. Layer Meteorol. 107 (3), 581–603. https://doi.org/10.1023/A:1022880530523.

Zeng, X.B., Wang, A.H., 2007. Consistent parameterization of roughness length and displacement height for sparse and dense canopies in land models. J. Hydrometeorol. 8 (4), 730–737. https://doi.org/10.1175/Jhm607.1.

Zhao, L., Lee, X.H., Suyker, A.E., Wen, X.F., 2016. Influence of leaf area index on the radiometric resistance to heat transfer. Bound.-Layer Meteorol. 158 (1), 105–123. https://doi.org/10.1007/s10546-015-0070-4.